Monthly Notices
of the
ROYAL ASTRONOMICAL SOCIETY

MNRAS **437,** 862–878 (2014)
Advance Access publication 2013 November 13

doi:10.1093/mnras/stt1949

Cold gas dynamics in Hydra-A: evidence for a rotating disc

S. L. Hamer,[1,2]★ A. C. Edge,[1] A. M. Swinbank,[1] J. B. R. Oonk,[3] R. Mittal,[4] B. R. McNamara,[5] H. R. Russell,[5] M. N. Bremer,[6] F. Combes,[2] A. C. Fabian,[7] N. P. H. Nesvadba,[8] C. P. O'Dea,[9] S. A. Baum,[4] P. Salomé,[2] G. Tremblay,[10] M. Donahue,[11] G. J. Ferland[12] and C. L. Sarazin[13]

[1]*Institute for Computational Cosmology, Department of Physics, Durham University, South Road, Durham DH1 3LE, UK*
[2]*LERMA Observatoire de paris, CNRS, 61 rue de l'Observatoire, F-75014 Paris, France*
[3]*ASTRON, Netherlands Institute for Radio Astronomy, PO Box 2, NL-7990 AA Dwingeloo, the Netherlands*
[4]*Chester F. Carlson Center for Imaging Science, 54 Lomb Memorial Drive, Rochester, NY 14523, USA*
[5]*Department of Physics and Astronomy, University of Waterloo, Waterloo, ON N2L 3G1, Canada*
[6]*H H Wills Physics Laboratory, Tyndall Avenue, Bristol BS8 1TL, UK*
[7]*Institute of Astronomy, University of Cambridge, Madingley Road, Cambridge CB1 0HA, UK*
[8]*Institut d'Astrophysique Spatiale, CNRS, Université Paris-Sud, F-91405 Orsay, France*
[9]*School of Physics and Astronomy, RIT, 84 Lomb Memorial Dr., Rochester, NY 14623, USA*
[10]*European Southern Observatory, Karl-Schwarzschild-Str. 2, D-85748 Garching bei München, Germany*
[11]*Physics and Astronomy Department, Michigan State University, East Lansing, MI 48824, USA*
[12]*Department of Physics, University of Kentucky, Lexington, KY 40506, USA*
[13]*Department of Astronomy, University of Virginia, Charlottesville, VA 22904-4325, USA*

Accepted 2013 October 9. Received 2013 October 8; in original form 2013 April 11

ABSTRACT

We present multifrequency observations of the radio galaxy Hydra-A (3C218) located in the core of a massive, X-ray luminous galaxy cluster. Integral field unit spectroscopy is used to trace the kinematics of the ionized and warm molecular hydrogen which are consistent with an ∼5 kpc rotating disc. Broad, double-peaked lines of CO(2–1), [C II] 157 μm and [O I] 63 μm are detected. We estimate the mass of the cold gas within the disc to be $M_{\rm gas} = 2.3 \pm 0.3 \times 10^9$ M$_\odot$. These observations demonstrate that the complex line profiles found in the cold atomic and molecular gas are related to the rotating disc or ring of gas. Finally, a *Hubble Space Telescope* image of the galaxy shows that this gas disc contains a substantial mass of dust. The large gas mass, star formation rate and kinematics are consistent with the levels of gas cooling from the intracluster medium (ICM). We conclude that the cold gas originates from the continual quiescent accumulation of cooled ICM gas. The rotation is in a plane perpendicular to the projected orientation of the radio jets and ICM cavities hinting at a possible connection between the kpc-scale cooling gas and the accretion of material on to the black hole. We discuss the implications of these observations for models of cold accretion, AGN feedback and cooling flows.

Key words: galaxies: clusters: individual: Hydra-A – galaxies: clusters: intracluster medium – galaxies: elliptical and lenticular, cD.

1 INTRODUCTION

The symbiotic relationship between the brightest cluster galaxy (BCG) and the dense intracluster medium (ICM) that surrounds it has important implications for our understanding of the formation and evolution of massive galaxies within the cores of clusters (see Fabian 2012; McNamara & Nulsen 2012 for reviews). The energetics of the gas show that the different gas phases are connected, for instance the close correlation between the X-ray properties (cooling time, central entropy, etc.) of the cluster core and the detection of optical lines (Crawford et al. 1999) in the BCG as shown by Cavagnolo et al. (2008) and Sanderson, Edge & Smith (2009). Hence, the implicit connection of the optical emission to the cold (Edge 2001; Salomé & Combes 2003) and warm (Edge et al. 2002; Egami et al. 2006; Donahue et al. 2011) molecular gas suggests that there is a direct link between the rapidly cooling gas in the ICM ($t_{\rm cool} < 10^9$ yr) and the presence of cold molecular gas. However, any model positing that the cool gas in the BCG condenses from the hot ICM must also satisfy stringent observational constraints on the

★E-mail: stephen.hamer@obspm.fr

rate of energy loss from gas at temperatures above $\sim\frac{1}{3}T_{\rm cluster}$ and strong limits on cooling of gas below that temperature (Peterson et al. 2001; Sanders et al. 2010). AGN in the BCG may supply the heat required to curtail radiative cooling. While the global AGN energy budget seems sufficient, the details of how the AGN prevents the ICM from rapidly cooling are not yet settled (Fabian 2012; McNamara & Nulsen 2012).

Feedback of energy from AGN outbursts has been invoked both to provide a potential source of the heating required to truncate the cooling of the ICM and to resolve the overproduction of massive galaxies in semi-analytic models (Bower et al. 2006; Croton et al. 2006). This AGN feedback injects mechanical energy into the ICM as outflows from the black hole inflate kpc-scale cavities in the X-ray atmosphere (McNamara & Nulsen 2007). One of the most striking examples of these cavities is Hydra-A (3C218; McNamara et al. 2000; Wise et al. 2007), which has clearly defined X-ray surface brightness depressions in the ICM that spatially correlate to the complex radio structure in this radio source. Hydra-A is the central galaxy of an X-ray luminous cluster which exhibits strong optical line emission showing a complex velocity structure that clearly indicates evidence of rotation (Simkin 1979; Ekers & Simkin 1983; Melnick, Gopal-Krishna & Terlevich 1997) and dust (Hansen, Jorgensen & Norgaard-Nielsen 1995). McNamara (1995) identified the presence of excess blue light from the central $\sim$8 arcsec $\times$ 6 arcsec (8.4 $\times$ 6.3 kpc) region which is spatially coincident with the rotating emission line nebula. This region has a major axis which in projection is aligned almost perpendicularly to the radio jet axis and suggests the presence of a young stellar population within the rotating ionized gas which they attribute to locally enhanced star formation fuelled by either the cooling flow or infalling material. McNamara (1995) also noted that this configuration is similar to the standard model of AGN disc accretion, although the scales involved in this system are much greater.

Hydra-A shares many properties with the archetypal central galaxy in a cooling flow cluster, NGC 1275/Perseus-A (Fabian et al. 1981), which is a powerful radio galaxy with multiple cavities created by repeated AGN outbursts (Böhringer et al. 1993; Fabian et al. 2003a). The detection of H I absorption (Dwarakanath, van Gorkom & Owen 1994; Dwarakanath, Owen & van Gorkom 1995; Taylor 1996), CO line emission (Salomé & Combes 2003), polycyclic aromatic hydrocarbon features (Donahue et al. 2011) and warm H_2 rovibrational and rotational lines (Jaffe & Bremer 1997; Edge et al. 2002; Donahue et al. 2011) in both Hydra-A and NGC 1275 all suggest a significant mass of atomic and molecular gas at a range of temperatures in the core of both galaxies. The dynamics of this phase and its relationship with the optical lines and associated star formation are open issues given that most observations are from a single dish or single line of sight.

In this paper, we present new data over sub-mm to optical wavelengths that shed new light on the nature and dynamics of the cold gas in Hydra-A. In particular, new data from *Herschel* (Pilbratt et al. 2010) and Institut de RadioAstronomie Millimétrique (IRAM) 30 m combined with Very Large Telescope (VLT) integral field data provide a much clearer picture of the dynamics of the cold gas. In Section 2, we outline our observations and analysis techniques. Next we outline our results (Section 3) before discussing their implications in Section 4. Finally, a summary and conclusions are reported in Section 5. We assume $\Omega_{\rm m} = 0.27$, $\Lambda = 0.73$ and $H_0 = 71\,{\rm km\,s^{-1}\,Mpc^{-1}}$ throughout. In this cosmology, the luminosity distance of the source is 242 Mpc, and 1 arcsec corresponds to a physical scale of 1.053 kpc at the redshift of Hydra-A 0.054 878 (Smith et al. 2004).

2 OBSERVATIONS AND DATA REDUCTION

2.1 VIMOS

Optical integral field unit (IFU) observations of Hydra-A were taken using the VIMOS (Visible Multi-Object Spectrograph) instrument on the 8.2 m VLT in 2007 October [programme ID 080.A-0224(A)]. Three 600 s exposures were taken with a pointing dither included between each exposure to minimize the effect of bad pixels. The HR_Orange grism and GG435 filter (spectral resolution of $R \sim \Delta\lambda/\lambda \sim 2650$ over the wavelength range 5250–7400 Å) were used to observe Hα ($\lambda_{\rm rest} = 6562.8$ Å) at the redshift of the cluster. The observations were taken in moderate seeing conditions with a mean seeing of $\sim$1.25 arcsec.

We reduced the raw data using the ESOREX package. We performed the basic data reduction including bias subtractions, flat-fielding and the wavelength and flux calibrations. In order to prepare the data for sky subtraction, we masked any point-like objects to remove any stars within the field. The BCG was then removed from the field by masking all pixels within an isophote of half the peak flux. This level was chosen empirically as the best compromise to allow a good sampling of sky pixels while removing the majority of the BCG light. The sky level for each quadrant is then the median value of the remaining pixels at each wavelength increment. This sky spectrum was then subtracted from each pixel in the four quadrants before they were combined into a single data cube. The more extended galaxy contribution which was included in the sky spectrum is from stellar continuum and thus relatively flat. As our analysis is concentrated solely on the line emission, this slight oversubtraction has a minimal effect on the results presented here. Finally, we median-combined the three exposures for each pointing in order to eliminate cosmic rays. To mosaic the three pointings, we determined the exact position of the BCG (the peak of the smoothed continuum flux) in each observation and combine them centring on this position to create a cube with an $\sim$29 arcsec $\times$ 28 arcsec field of view.

2.2 SINFONI

The SINFONI (Spectrograph for Integral Field Observations in the Near Infrared) instrument on the VLT was used to take *H*- and *K*-band IFU observations of Hydra-A (programme 082.B-0671, PI: Nesvadba) in 2008 November and 2009 February. The observations consist of three visits in each band, with each visit comprising six 300 s exposures, four centred on the BCG and two on an offset sky region. The observing conditions were better than those of the VIMOS observations with a mean seeing of $\sim$0.59 arcsec.

The ESOREX package was set up for SINFONI IFU observations and used to reduce these data. We corrected for dark current, the linearity of the detector, optical distortions between the slitlets and performed the basic calibration steps as for VIMOS. The sky reduction was also performed using this package for the separate sky observations taken during each pointing. The individual pointings in each band were then combined into a single cube in the same manner as the VIMOS observations. This procedure produced cubes with an $\sim$8 arcsec $\times$ 8 arcsec field of view.

2.3 Analysis of the IFU data

The spectral cubes produced by the reduction processes were unwrapped into two-dimensional spectral images so that the presence of emission lines could be identified by eye. Spectral models consisting of Gaussian emission lines and a flat continuum were

fitted to each line at each spatial position so that maps of the spectral properties could be produced. The fitting was performed on a small region of the spectrum around the line to enable the fitting routine to work more effectively. This region corresponded to 160 Å (240 wavelength elements) for VIMOS and 490 Å (200 wavelength elements) for SINFONI. The noise level was calculated using a second such region near the first that contained no emission lines or sky features.

The median value of the spectrum within the extracted region was taken as a continuum model against which to compare a fit to the line. The fits to the line were made using Gaussian models in which the parameters were allowed to vary. These fits were accepted when they provided a 7σ better fit than the flat continuum alone. The primary fit to the VIMOS data was to the Hα/[N II] triplet. The models were fitted to the rest wavelength of the line and the redshift was allowed to vary; the three lines relative to rest-frame positions were fixed. The total flux in the Hα line and strong [N II]$\lambda_{\rm rest}$ 6583 Å line were allowed to vary independently; the flux in the weaker [N II] line was set at one third of the flux of the brighter line. The line widths [full width at half-maximum (FWHM), deconvolved for instrumental resolution] were allowed to vary between pixels but the [N II] was forced to have the same width as the Hα. The continuum was typically 'flat' over the short wavelength ranges being studied. As such the continuum level was set to a constant value throughout each spectral model. However, the value was allowed to vary between spatial resolution elements. In lower flux regions where a 7σ fit could not be obtained, the routine binned the surrounding 8 pixels and attempted the fit again. Such binning may combine regions with different central velocities which can artificially broaden the lines. This effect will be largest in regions with a high velocity gradient; we highlight the cases where this may be a problem in the text.

In the SINFONI observations, the brightest lines are from Paschen α (Paα) and molecular hydrogen. The rest-frame wavelengths of these lines are sufficiently separated to allow each line to be fitted independently from the other lines. A single-Gaussian model was fitted to the line at the rest wavelength, and the redshift, flux, width (FWHM, deconvolved for instrumental resolution) and continuum level were allowed to vary. Again, the routine binned pixels together in the event that a 7σ fit could not be obtained. When a line was detected in this way, the single-Gaussian model (or the triplet in the case of Hα and [N II]) was tested against a two-component model to check for extra velocity components. This second Gaussian was varied independently of the other model (central redshift, intensity and line width) and was allowed to be much broader. When all the parameters were re-minimized, the χ^2 of the new fit was calculated and compared to the original models. Although this provided a better fit to the data, the extra components were not found to be significant due to the reduction of the degrees of freedom.

2.4 IRAM 30 m

We obtained IRAM 30 m data for the CO(1–0) and CO(2–1) lines in Hydra-A in 2010 April at 109.274 and 218.545 GHz, respectively. The observations were performed simultaneously in exceptional conditions ($\tau_{230\,\rm GHz} \sim 0.05$) with the Eight MIxer Receiver (EMIR) using a 4 GHz bandwidth covering each line (Carter et al. 2012). The observation was of 2 h duration with wobbler switching with a 90 arcsec throw. The observations reached a noise level of 0.35 and 0.30 mK in 100 km s^{-1} channels for CO(1–0) and CO(2–1), respectively. The unusual situation of obtaining a better temperature sensitivity at CO(2–1), combined with a beam of a quarter the size compared to CO(1–0), means that there is a highly significant CO(2–1) detection but at best a marginal one for CO(1–0). Both the Wideband Line Multiple Autocorrelator (WILMA) and 4 MHz backends were used to sample the data, but in this paper we present only the CO(2–1) spectrum taken with the WILMA backend as they were the most stable and provide the most reliable CO detection.

2.5 *Herschel*

Hydra-A was observed with *Herschel* as part of an open time key project (OTKP) to observe a statistical sample of cooling flow clusters (programme OTKP_aedge1, PI: Edge). We used the Photodetector Array Camera and Spectrometer (PACS) instrument to obtain spectral observations of the two principal atomic cooling lines, [O I] (OD:536, OBSID:1342207793) and [C II] (OD:538, OBSID:1342207817) at 63 and 157 μm, respectively. The lines were observed in line spectroscopy mode using the chopping and nodding implementation to account for the background and dark current. These were then analysed using the standard pipeline routines included in the latest release of the Herschel Interactive Processing Environment (HIPE v. 7.1.0). A detailed description of the *Herschel* data reduction can be found in Mittal et al. (2011). The full analysis of these spectral data and the additional PACS and Spectral and Photometric Imaging Receiver (SPIRE) photometry will be made elsewhere (Oonk et al., in preparation).

2.6 *HST*

A *Hubble Space Telescope* (*HST*) Advanced Camera for Surveys (ACS) image of Hydra-A was obtained on 2011 April 16 using ACS with the Wide Field Camera (WFC) detector and *F*814*W* filter for an exposure time of 2367 s. A 2709 s UV image was obtained with *HST* ACS on 2011 April 11 using the Solar-Blind Camera (SBC) detector and the *F*140*LP* filter. Standard calibrations were then applied including subtraction of the bias, correcting for dark current and flat-fielding. This observation was taken as part of a programme to obtain high-resolution imaging of all the *Herschel* OTKP clusters (Proposal ID 12220, PI: Mittal).

3 RESULTS

3.1 IFU maps

In Fig. 1, we show the *HST* optical (*F*814*W*) and UV (*F*140*LP*) images of Hydra-A. The optical image shows the position of the H_2(1–0) S(1) and radio emission while the UV image has contours of the Paα. It is apparent from this image that there is a surface brightness depression running across the BCG at $\sim -70^\circ$ to the north–south line. The Paα line flux is contoured on this plot and clearly shows the Paα emission to be consistent with the position and orientation of the dust lane. The IFU maps for the Hα line are displayed in Fig. 2; we show the continuum, line flux, relative velocity and FWHM in panels A, B, C and D, respectively. The VIMOS Hα flux map shows a bright elongated region which is coincident with and shares the same PA as the Paα and dust lane as shown in Fig. 1. Lower surface brightness Hα emission is also present extended to the north and south of the BCG. Although this emission is of lower surface brightness, it is still detected at well above 7σ and is present in the narrow-band image of McDonald et al. (2010), suggesting that it is not the result of noise. Its extent follows the direction of the radio jets suggesting that the two are

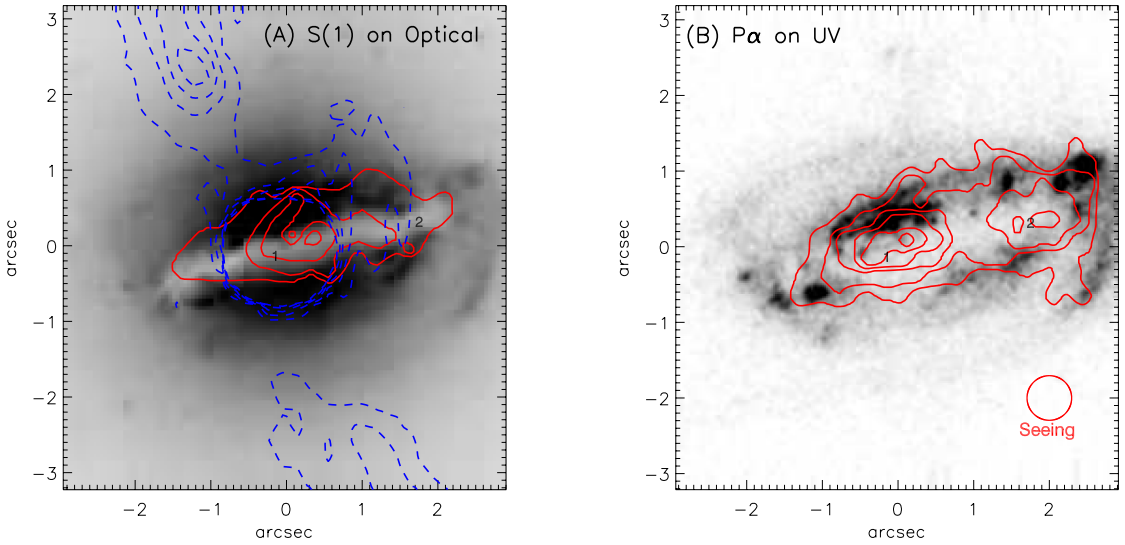

Figure 1. Panel (A) presents an *HST F*814*W* optical image of Hydra-A showing a clear dust lane across the centre of the BCG. Contoured over this as solid lines is the S(1) intensity which can be seen to run along the length of the dust lane. The dashed lines show the radio emission with central point source removed. The radio jets can be seen extending to the north-east and south-west of the BCG, almost perpendicular to the dust lane in projection. Panel (B) presents an *HST F*140*LP* UV image of Hydra-A which shows a clumpy structure indicating regions of localized star formation. The intensity of the emission from the Paα line is contoured and shows a similar position and structure to the S(1). A depression in the UV can be seen at the position of the dust lane suggesting that some star formation may be obscured at UV wavelengths. The numbers on the two images match the centroids of the two Paα peaks and the position (0,0) corresponds to the centre of the BCG in optical light.

possibly related. In systems with cavities, it is common to see Hα emission associated with the enhanced X-ray emission surrounding cavities (for example Abell 2052 in McDonald et al. 2010) so this may be a similar effect.

The Hα velocity map shows a continuous velocity gradient across the BCG of $\sim$600 km s^{-1}. This velocity gradient runs across the BCG along the major extent of the dust lane. We note that the extended emission to the north and south is slightly blueshifted from the velocity of the BCG but is constant and consistent with the median velocity of the Hα emitting gas. The line width (all line widths quoted are FWHM deconvolved for instrumental resolution unless otherwise stated) of the emission in the central 1.2 $\times$ 1.2 arcsec^2 of the BCG is 300 $\pm$ 15 km s^{-1} and falls to 250 $\pm$ 13 km s^{-1} at the edges of the region containing the velocity gradient. The lower surface brightness extensions to the north and south have lower and more uniform line widths of 150 $\pm$ 16 km s^{-1}.

Fig. 3 shows a *K*-band continuum image produced by collapsing the *K*-band SINFONI observation over a region free of telluric absorption (2.07–2.32 µm). The dust lane seen in the optical image is also present in the NIR but is much less prominent due to the weaker dust absorption and the emission from a point source at the centre of the BCG. The Paα map shows emission elongated across the galaxy in the same direction as the dust lane. The emission shows a two-component structure with a depression in the Paα emission separating two bright components. Assuming a temperature of the ionized gas of 10^4 K, the mass of ionized hydrogen in a system can be estimated from the Paα flux (Oonk et al. 2010) as

$$M_{\rm H\,II} = 2.41 \times 10^{18} \left(\frac{F_{\rm Pa\alpha}}{\rm erg\,s^{-1}\,cm^{-2}}\right)\left(\frac{D}{\rm Mpc}\right)^2 \times \left(\frac{n_{\rm e}}{\rm cm^{-3}}\right)^{-1} {\rm M}_\odot, \quad (1)$$

where $F_{\rm Pa\alpha}$ is the Paα flux, D is the distance in Mpc and $n_{\rm e}$ is the electron number density. Assuming an electron density of $n_{\rm e}$ = 200 cm^{-3} as in Oonk et al. (2010), a distance of 242 Mpc and the measured Paα flux of 6.31 $\pm$ 0.39 $\times$ 10^{-14} erg s^{-1} cm^{-2}, we find an H II mass of 4.5 $\pm$ 0.28 $\times$ 10^7 M$_\odot$. The Paα shows a similar velocity structure to the Hα with a continuous gradient of $\sim$500–600 km s^{-1} running across the emission. The line width (FWHM) of the Paα is higher in the central 1.2 $\times$ 1.2 arcsec^2 of the emission (330 $\pm$ 39 km s^{-1}) than on the edges (150 $\pm$ 17 km s^{-1}). This is similar to the line-width variation seen in the Hα except that the FWHM at the edges is substantially lower. We note however that the lower spatial resolution of the VIMOS observations makes the Hα FWHM more responsive to broadening by the high velocity gradient in this system. The velocity width seen in the two ionized lines is consistent with observing through a rotating disc where we sample less random velocity components through the edge of the disc than through the centre. However, our current observations are not sufficiently detailed to fully constrain the emissivity within the disc to determine if it is continuous or there are gaps in the density that imply that the gas is in a ring.

The H_2 (1–0) S series lines sample the warm (1–2 $\times$ 10^3 K) vibrationally excited molecular gas within the BCG. Within the *K*-band spectrum of Hydra-A, we find four strong lines associated with the molecular gas, H_2 (1–0) S(0) to S(3) (Fig. 4 shows the fits to all four H_2 (1–0) S lines). The S(1) line emission is shown in the second row of Fig. 4. It is the most reliably characterized of the molecular lines due to being strong and isolated from other lines and telluric features. For consistency with the other molecular lines however, we present a map of the fits to emission above the 5σ significance level. The S(1) emission shows a clear extent, matching that seen in the Paα and dust lane. In contrast, however, the S(1) flux map does not show the double-component structure seen in the Paα. However, the velocity structure of the S(1) matches that seen in the ionized lines with a clearly visible velocity gradient of $\sim$600 km s^{-1} running along the long axis of the emission. The FWHM of the S(1) emission peaks at 346 $\pm$ 96 km s^{-1} in the central 1.2 $\times$ 1.2 arcsec^2 of the BCG. This width is higher than that seen in

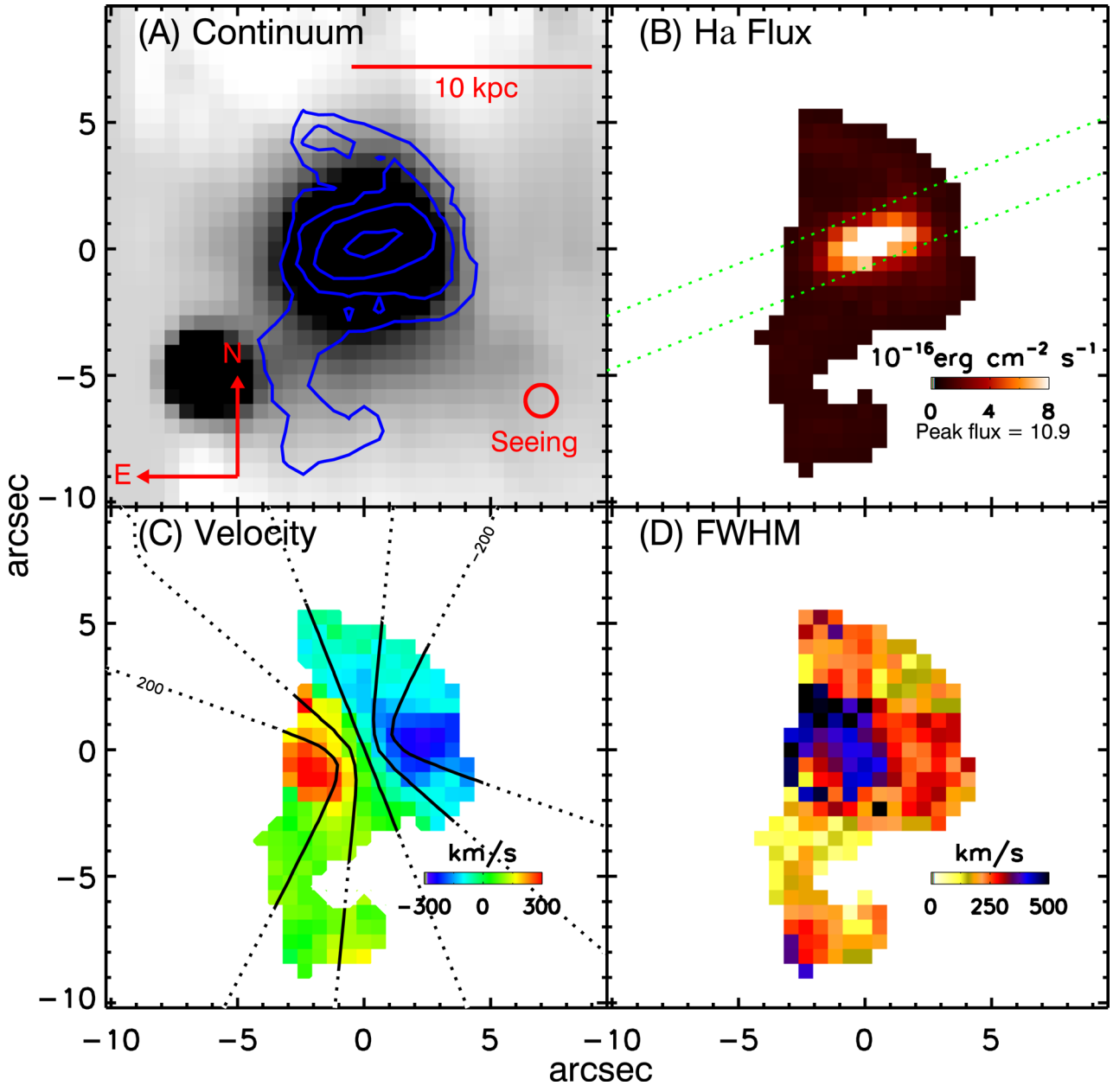

Figure 2. The IFU maps of the Hα emission as taken from fits to the Hα/[N II] triplet observed in the VIMOS cubes. Panel (A) shows a continuum image made by collapsing the cube; the contours show the Hα emission clearly centred on the BCG. Panel (B) shows an Hα flux map which shows a disc of bright emission running across the BCG. In panel (C), we show the relative velocity of the Hα line to the galaxy redshift; a strong velocity gradient of $\sim$600 km s^{-1} can clearly be seen. Contoured on this plot are lines of constant velocity created by fitting a disc model to the velocity map. The final panel (D) shows the measured FWHM of the line which can be seen to broaden at the centre of the velocity gradient.

the Paα and Hα but is consistent within the errors. The width falls to 200 $\pm$ 55 km s^{-1} at the edges which is consistent with both the ionized lines.

The mass of warm molecular hydrogen can be estimated from the H_2 (1–0) S(1) flux using equation 4 from Oonk et al. (2010), assuming a single kinetic temperature of $T_{\rm vib} = 2000$ K and a transition probability of 3.47 $\times$ 10^{-7} s^{-1}, as

$$M_{\rm H_2} = 5.08 \times 10^{13} \left(\frac{F_{\rm H_2(1-0)\ S(1)}}{\rm erg\,s^{-1}\,cm^{-2}}\right)\left(\frac{D}{\rm Mpc}\right)^2 {\rm M}_\odot, \quad (2)$$

where $F_{\rm H_2(1-0)\ S(1)}$ is the flux in the S(1) line and D is the distance in Mpc. Again using a distance of 242 Mpc and the measured $F_{\rm H_2(1-0)S(1)}$ flux of 142 $\pm$ 27 $\times$ 10^{-16} erg s^{-1} cm^{-2}, we find an H_2 mass of 4.2 $\pm$ 0.8 $\times$ 10^4 M$_\odot$.

The S(3) line (Fig. 4, row four) is another strong molecular line. However, its position in the spectrum places it near a strong telluric feature. The removal of this telluric feature results in an increase in noise compared to other parts of the spectrum. While the line is clearly detected at greater than the 5σ significance limit, the physical properties derived from the fit are less reliably determined than those of the S(1) line. We also note that in the nuclear regions, the S(3)

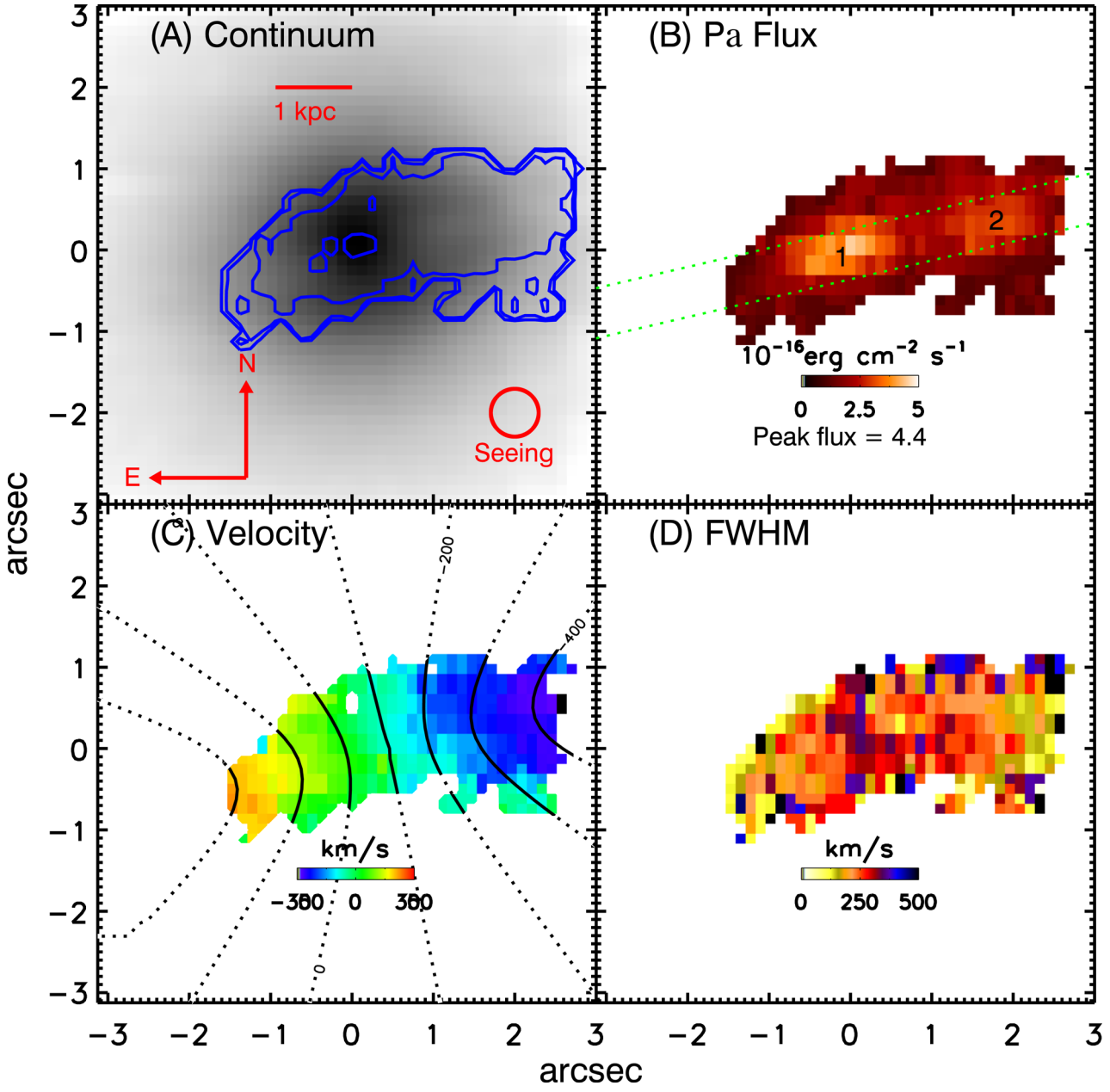

Figure 3. The IFU maps of the Paα emission as taken from fits to the Paα emission line observed in the SINFONI cubes. Panel (A) shows a continuum *K*-band image created by collapsing the cube with contours of the Paα emission. In panel (B), we show a Paα flux map which shows an elongated structure across the BCG. In panel (C), we show the relative velocity of the Paα line to the galaxy redshift; a strong velocity gradient of $\sim$600 km s^{-1} can be seen extending over $\sim$4 arcsec (with 1 arcsec $\sim$1.05 kpc) along a similar PA to the Hα. Contoured on this plot are lines of constant velocity created by fitting a disc model to the velocity map. The final panel (D) shows the measured FWHM of the line which seems fairly uniform.

emission appears to be blended with He I emission, requiring that the two lines have been fitted together with a fixed rest wavelength separation. The velocity profile of the S(3) line is consistent with that from the other molecular lines and ionized lines presented so far, with a velocity gradient of $\sim$500–600 km s^{-1} running along the direction of the dust lane. The line width of S(3) is mostly consistent with that of S(1) peaking at 375 $\pm$ 80 km s^{-1} in the central 1.2 $\times$ 1.2 arcsec^2 of the emission and falling to 230 $\pm$ 72 km s^{-1} at the edges.

Of the molecular hydrogen lines, S(0) is the least reliable since it is located at the noisy red edge of the spectrum. As such, fits could only be obtained at the 5σ significance level for this line.

The S(0) fits (Fig. 4, row one) do not show as extreme a velocity gradient as seen in the Paα but they do show a similar velocity structure with a continuous velocity gradient running almost east to west across the emission. We note that the S(0) emission is not as extended (likely due to lower signal-to-noise) along this direction as the other *K*-band lines which may account for this. The FWHM of the S(0) line is highest at a position centred on the peak of the emission, which is consistent with being at the centre of the BCG. The FWHM in the central 1.2 $\times$ 1.2 arcsec^2 is 308 $\pm$ 104 km s^{-1}. However, the map shows regions of similar line width throughout the structure. The similarity of line widths is possibly due to blending with noise spikes that artificially broaden the line fit.

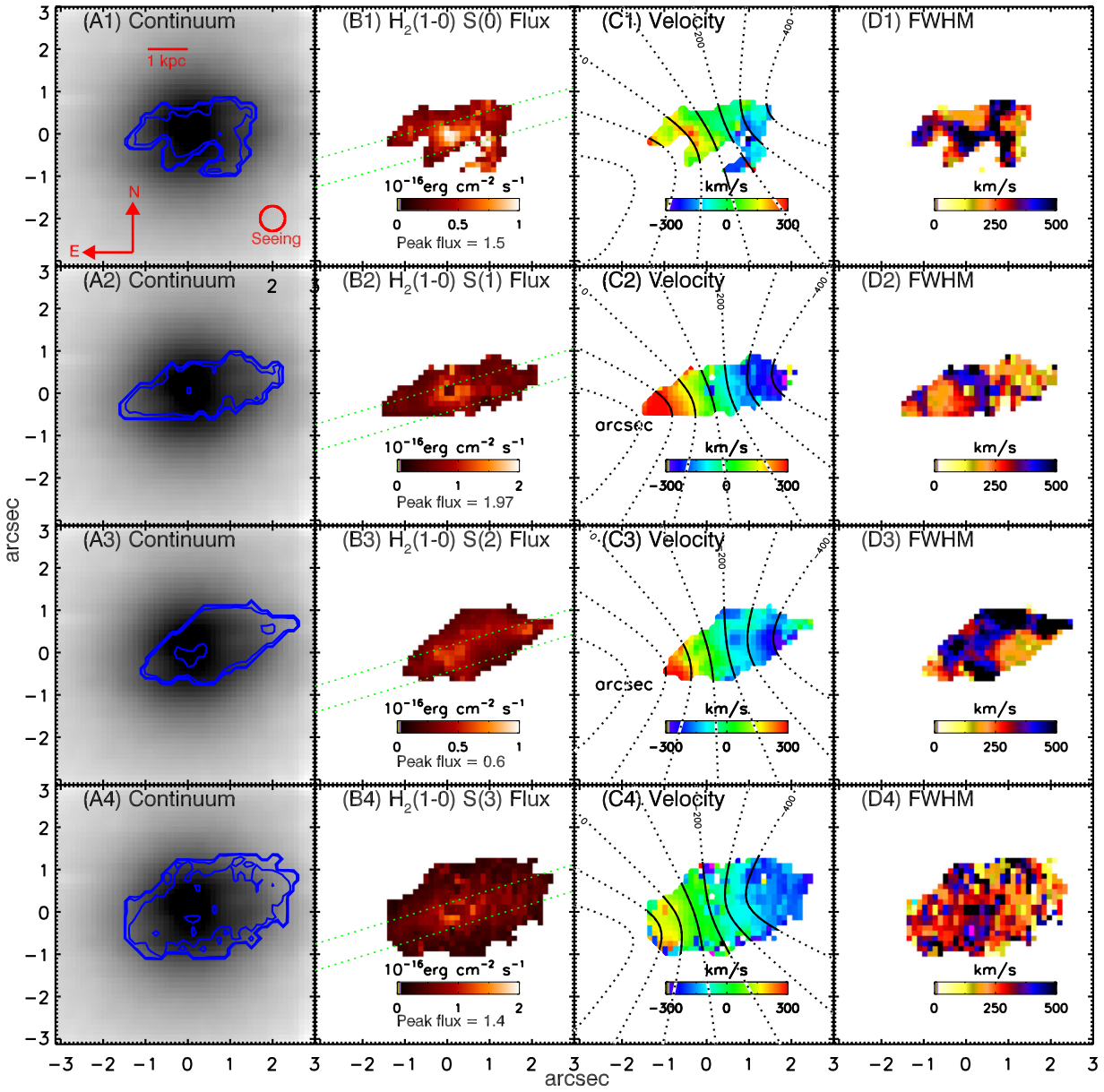

Figure 4. The IFU maps of the H_2(1–0) S(0) to S(3) emission as taken from fits to the emission lines observed in the SINFONI cubes. From top to bottom, the panels are arranged in order from S(0) to S(3). The far-left panels (A) show a continuum *K*-band image created by collapsing the cube with a flux map for each line contoured in blue. The centre-left panels (B) show the flux maps which typically show an elongated structure across the BCG. The dotted lines in these panels show the region from which the rotation curves were extracted and represent the position angle of the disc as determined by the disc fitting. In the centre-right panels (C), we show the relative velocity of each emission line to the galaxy redshift. A strong velocity gradient of $\sim$600 km s^{-1} can be seen along a similar PA to the Hα. Contoured on these plots are lines of constant velocity created by fitting a disc model to the velocity maps. The far-right panels (D) show the measured FWHM of the lines. Each line shows an increase in the FWHM at the point where the flux map appears brightest; for the S(1) and S(3) lines this point also matches the dynamical centre (the point at which the velocity of the disc model goes through 0). However the S(0) and S(2) lines also show enhanced line width along the edges of the emission, though this is likely a result of the lower signal-to-noise and therefore not real. The consistency of the velocity structure of these lines with those of the ionized Hα and Paα suggests that the warm molecular gas occupies the same rotating disc as the ionized gas.

The S(2) emission is shown in the third row of Fig. 4. While the S(2) emission from Hydra-A was weaker than the S(0), its observed wavelength put it in a significantly less noisy part of the spectrum resulting in the detection of more emission at 5σ. As such its structure more closely matches that of the S(1), suggesting that the structure in the S(0) map is likely the result of incompletely detected emission and is not real. As expected from the other molecular lines, the velocity structure of the S(2) emission matches that of the ionized gas with an $\sim$600 km s^{-1} gradient running along the line of the dust lane. The line width of S(2) appears considerably higher than the S(1). This is however likely a result of the binning used by the fitting procedure to obtain the required signal-to-noise. By binning together pixels at substantially different velocities before fitting, the line width can be artificially increased. The velocity gradient in the central regions is $\sim$30 km s^{-1} per pixel, thus binning 3 $\times$ 3 pixels can result in a broadening of the line of the order of 100 km s^{-1} which is consistent with the difference in line width observed. Consulting the integrated spectrum of the 1.2 $\times$ 1.2 arcsec^2 centred on

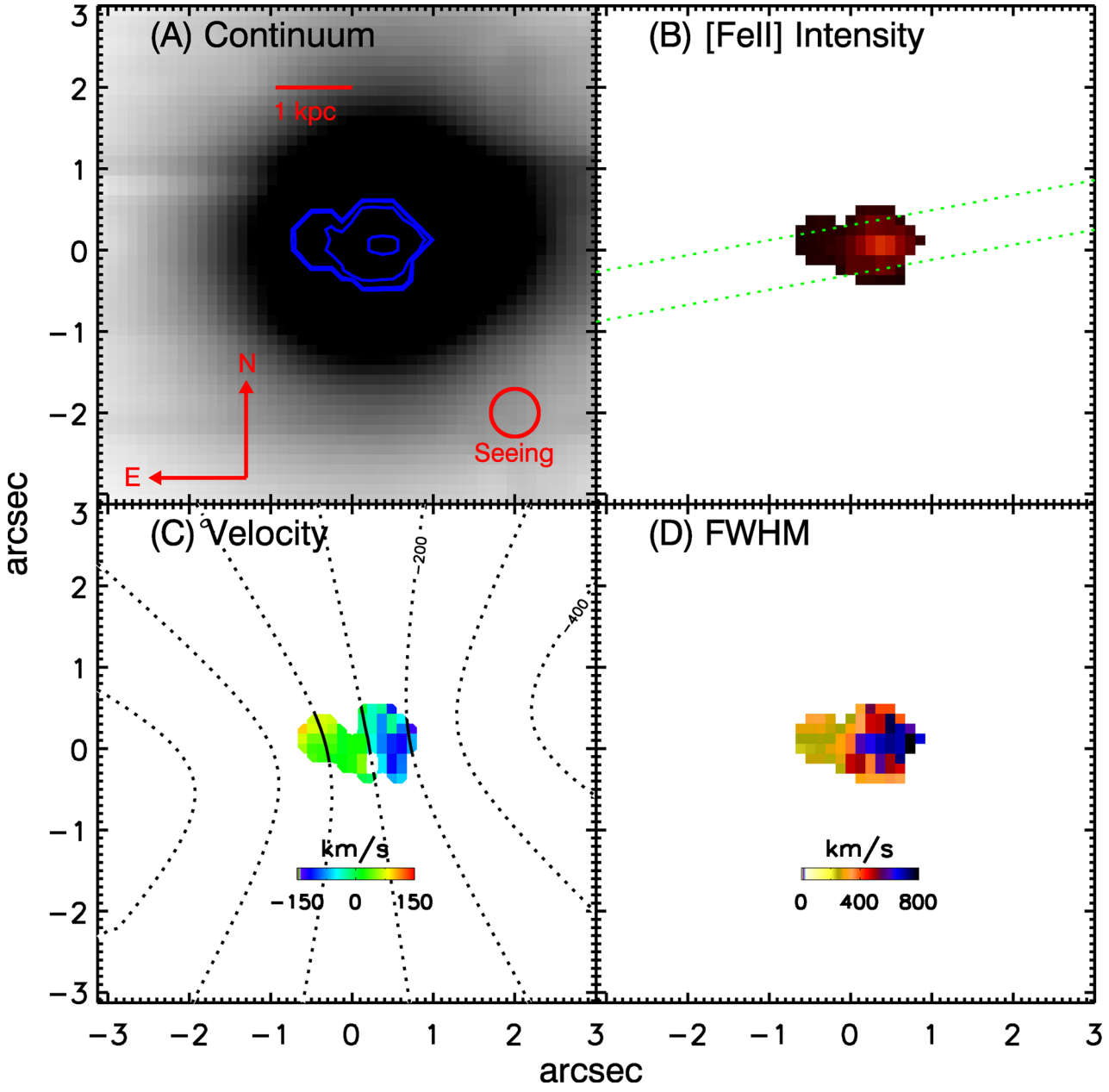

Figure 5. The IFU maps of the [Fe II] emission as taken from fits to the [Fe II] emission line observed in the SINFONI cubes. Panel (A) shows a continuum *K*-band image created by collapsing the cube with contours of the [Fe II] emission. In panel (B), we show an [Fe II] intensity map; it can be seen that the [Fe II] emission is much more centrally concentrated than the other lines, which is expected as it is associated with the highest density regions. In panel (C), we show the relative velocity of the [Fe II] line to the galaxy redshift; a strong velocity gradient of $\sim$200 km s^{-1} can be seen along a similar PA to the Hα. Contoured on this plot are lines of constant velocity created by fitting a disc model to the velocity map. It should be noted that the [Fe II] emission is barely resolved at just twice the seeing so this velocity gradient may not be real. The final panel (D) shows the measured FWHM of the line which shows a much broader profile in the central regions than the other lines.

the BCG suggests that the line width is consistent with that of the other lines (362 $\pm$ 70 km s^{-1}). As such there is no significant difference in the warm molecular line widths as is expected since they are emitted from the same gas.

The separate component seen in the Paα map does not appear in the (1–0) S series line emission. This non-detection is likely to be due to the lower signal-to-noise as the lines are present within the total spectrum of this region (extracted 1 $\times$ 1 arcsec^2 centred on the offset Paα peak) though the line is weak compared to Paα.

[Fe II] emission was the only line detected in the *H*-band observations. The maps presented in Fig. 5 show that the [Fe II] emission is compact and located at the centre of the BCG. The luminosity of [Fe II] emission has a high dependence on the gas density (Bautista, Pradhan & Osterbrock 1994) so we would expect it to be brightest in the central regions where the gas density is higher. Despite being compact the line does appear to be extended to the east on scales slightly greater than the seeing. Within this small extent, there appears to be a velocity change of $\sim$200 km s^{-1} across the

Table 1. [N II] and Hα have the same PA, inclination and velocity as they are fitted as a triplet. The transition radius is measured as the point at which the fit rotation curve begins to flatten. A suitable standard star for the [Fe II] was not taken so no value of the luminosity could be obtained. $V_{2.2}$ is defined as the inclination-corrected velocity at $R_{2.2}$, with the values of $R_{2.2}$ set to 3.2 and 2.20 kpc for VIMOS and SINFONI, respectively. The square brackets give the error on the last decimal place.

Properties of the seven emission lines fitted with disc models						
Line	Position angle (°)	Inclination (°)	Transition R (kpc)	Luminosity (10^{40} erg s^{-1})	$V_{2.2}$ (km s^{-1})	Redshift (At zero velocity)
Hα	-74 ± 3.0	56 ± 2.3	1.68 ± 0.26	14.22 ± 0.76	397 ± 49	0.054 39[12]
Paα	-77 ± 3.3	69 ± 2.0	1.97 ± 0.23	45.24 ± 2.83	341 ± 36	0.054 52[8]
H(1–0) S(0)	-66 ± 2.9	65 ± 2.0	1.46 ± 0.20	5.16 ± 1.11	384 ± 25	0.054 39[5]
H(1–0) S(1)	-74 ± 2.6	64 ± 2.9	1.48 ± 0.27	15.58 ± 5.94	381 ± 65	0.054 40[5]
H(1–0) S(2)	-78 ± 5.3	64 ± 3.6	1.76 ± 0.21	7.69 ± 1.14	369 ± 42	0.054 38[6]
H(1–0) S(3)	-73 ± 3.0	66 ± 2.7	1.54 ± 0.21	25.80 ± 1.34	421 ± 66	0.054 39[3]
[Fe II]	-80 ± 0.9	56 ± 1.8	1.70 ± 0.20	–	355 ± 33	0.054 73[10]

emission. This velocity gradient is consistent with that found from the other ionized and molecular lines across a similar extent. However, higher resolution observations of this emission are required to confirm if this velocity gradient is real. If it is, it presents a direct link between the gas on galaxy-wide scales and the nuclear region. The peak FWHM of the [Fe II] line is greater than that seen in the other lines, at $\sim$700 km s^{-1}, as would be expected if this emission came from the denser nuclear region. However, we note that the error on the line width is 349 km s^{-1} in this region. By contrast, the component extended to the east has a substantially lower width ($\sim 300 \pm 55$ km s^{-1}), which is more consistent with that seen in the molecular emission lines.

3.2 Rotation of the ionized gas

The ionized and warm molecular gas emission lines all show kinematics which are consistent with an ordered rotation. Disc models were fitted to the velocity maps shown above in order to determine the consistency of this rotation between the different lines. These disc models were constructed such that the velocity profile follows an arctan function. While this model is not physically motivated, it was found to be a good approximation of the velocity curve of disc galaxies by Courteau (1997). Table 1 gives the position angle (PA), inclination and transition radius of the disc as measured by these fits. The PA is measured from the north–south line counter-clockwise to the blueshifted end of the disc. The inclination is the angle of the plane of the disc relative to the plane of the sky with 0° corresponding to a face-on disc and 90° being an edge-on disc. Finally, the transition radius is the point at which the rotation curve begins to flatten. The fits find PA consistent to within $\sim$15° (Fig. 6) and rotation velocities consistent to within $\sim$60 km s^{-1} (within the spectral resolution of both instruments). The centre of rotation of each disc model differs slightly but all are consistent within the seeing of the observations ($\sim$0.5 arcsec). Given the small spatial scale of the [Fe II] emission compared to the seeing, there are very few uncorrelated data points in the disc fit so we constrained the disc model for [Fe II] to have an inclination and PA consistent with the other lines. We use the stellar sodium-D absorption feature ($\lambda_{\rm rest}$ 5895.92, 5889.95 Å) from a FOcal Reducer/low dispersion Spectrograph (FORS) observation to determine the central redshift of the BCG. From this fit, we find that the stellar component has a redshift of z =0.054 34[38], which is consistent within errors with the redshift at zero velocity for all lines. Combining the information from the seven lines suggests the presence of a disc of ionized and molecular gas in the centre of the Hydra-A BCG which is rotating with a peak-to-peak velocity of $\sim$700 km s^{-1} separated by 5 ± 0.7 kpc.

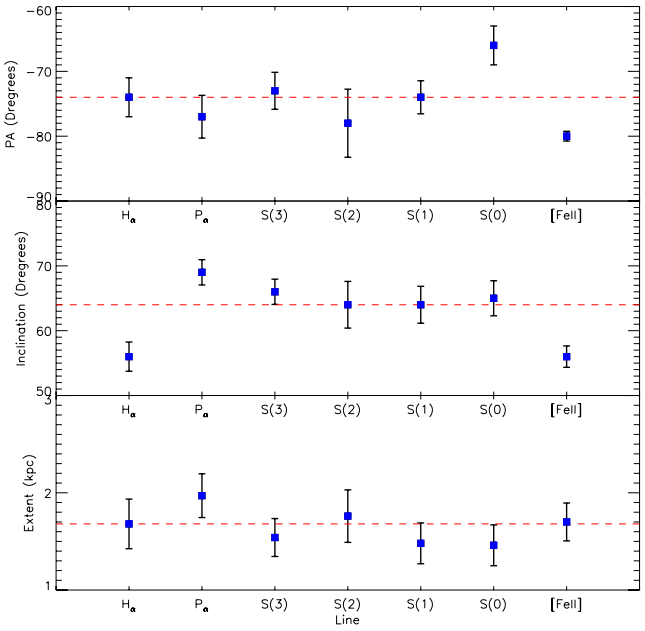

Figure 6. Comparison of the key parameters of the best fit for the disc model for each line. (Note that the rotation velocity comparison is shown later in Fig. 8.) The top panel shows a comparison of the PA, the middle shows the inclination angle and the bottom shows the distance at which the velocity curve turns over. The dashed line in each plot shows the median value. The errors are calculated from the Monte Carlo fitting routine and are the maximum deviation from the best-fitting parameters with a $\Delta\chi^2 < 1$ assuming that all other parameters are allowed to minimize. Note that the smaller error on the [Fe II] is a result of having to use more constrained limits on the parameters in order to get a fit. For each of these three parameters, the disc models show a good consistency between the lines.

Fig. 7 shows rotation curves extracted from the velocity maps along with profiles derived from the models using the same PA estimate, which was consistent for the disc models for each line. The extracted rotation curves all show little deviation from the models except at the edges where the line fits are not as precise due to the lower signal-to-noise. The S(0) line velocity profile appears less consistent with the model than the velocity profiles of the other molecular lines displayed in Fig. 7 and samples less of the velocity curve. However, as discussed in Section 3.1 the map of this line is

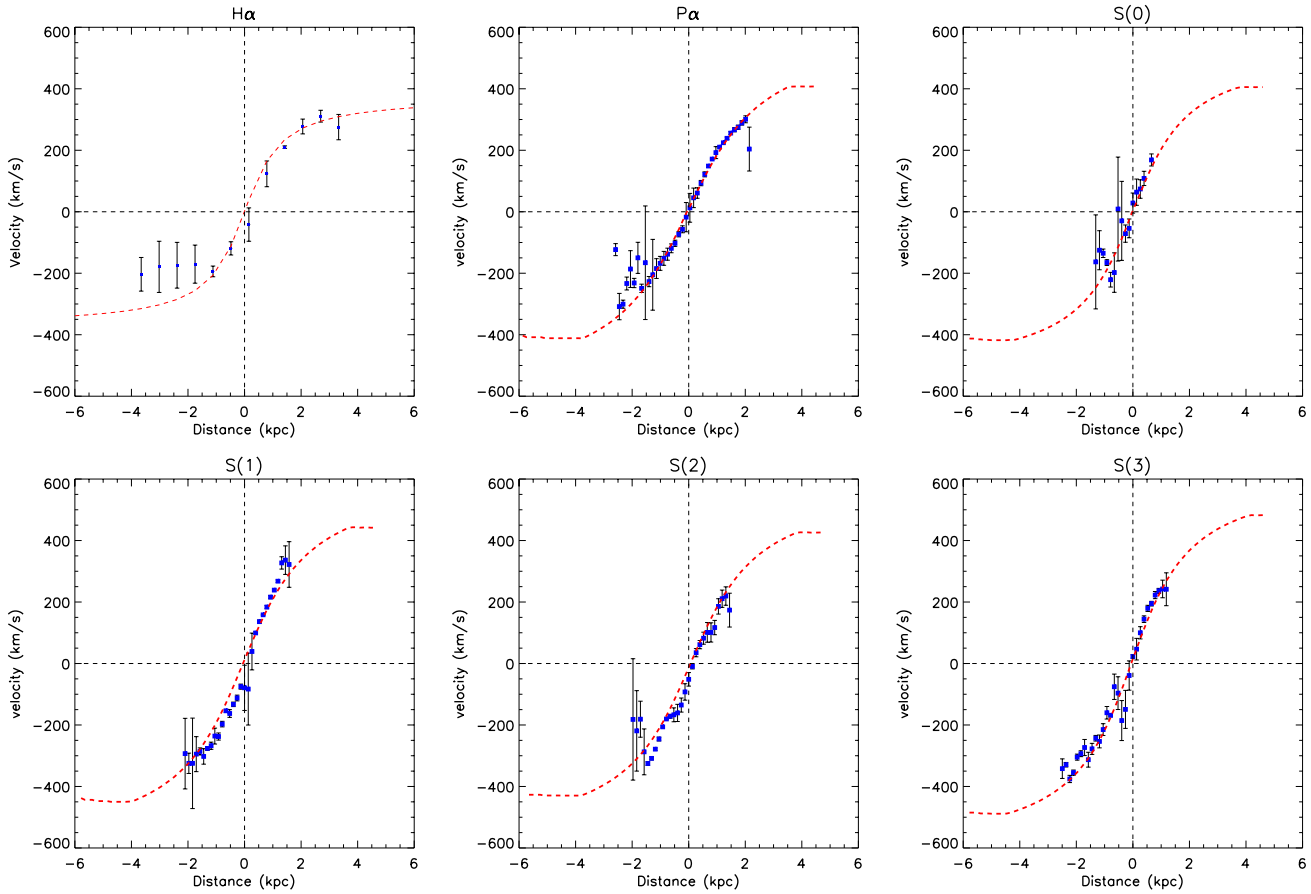

Figure 7. Velocity profiles for the six brightest lines from our VIMOS and SINFONI observations. The profiles are presented as observed (not inclination corrected); the errors are 1σ. The errors on the position (x-axis) are dominated by the seeing; these are not shown but are ∼1.3 kpc for the VIMOS (Hα) line and ∼0.5 kpc for SINFONI (other lines). The dashed line shows the velocity profile of the disc model taken along the same line as the data. For each line, the model provides a good fit to the data suggesting that the velocity is well fitted by a disc model; however, we note that for none of the lines do we reach the flattened part of the velocity profile.

noisier than the others and it is consistent with the model within errors. The Hα profile appears to be slightly offset from the model in the central regions (∼0.5 kpc at 0 km s^{-1}). However, we note that this is well within the positional error introduced by the poorer seeing of the VIMOS observation (∼1.3 kpc). Due to the [Fe II] line being barely resolved, we do not show its rotation curve. We note that the rotation curves in the inner ∼2 arcsec (2.1 kpc) appear rigid. Some caution is required in interpreting this as the seeing is of the order of 0.5 arcsec so this could be the effect of a smoothing of the rotation curve over these scales. However, it is suggestive that the mass density in the inner 2 kpc may be nearly constant rather than being proportional to the distance as it appears to be in the outer regions (beyond 2 kpc).

We use these rotation curves to directly constrain the dynamical mass of the BCG within the radius enclosing the disc. Assuming that the disc is purely exponential, then its surface brightness at radius r, $\Sigma_d(r)$ is given by

$$\Sigma_d(r) = \Sigma_0 \mathrm{e}^{\frac{-r}{r_s}}, \quad (3)$$

where Σ_0 is the central surface brightness and r_s is the disc scalelength. If the disc were purely exponential, the peak rotational amplitude should occur at a distance 2.2 times the disc scalelength (r_s) (Freeman 1970; Binney & Tremaine 1987). Using the inclinations calculated above, we produce surface brightness profiles of the VIMOS and SINFONI maps and fit lines of the form given in equation (3) to determine the disc scalelength. We then define the position $R_{2.2}$ as a distance from the centre of rotation equal to 2.2 times the disc scalelength and calculate the mass within this region (as in Miller et al. 2011). The inclination-corrected velocity at this point ($V_{2.2}$) is then used to calculate the dynamical mass within the disc. Fig. 8 compares the calculated value of $V_{2.2}$ for each line with the magnitude of the maximum velocity measured from the data. It can be seen that once corrected for inclination, the measured values agree with the calculated values of $V_{2.2}$ indicating that the data sample the disc out to $\sim R_{2.2}$. For the Hα emission, we find $R_{2.2} = 3.2$ kpc and $V_{2.2} = 397$ km s^{-1} which corresponds to a dynamical mass of $1.2 \times 10^{11}\,\mathrm{M}_\odot$. However, we note that the spatial resolution of the Hα map is 0.6 kpc. By contrast, the Paα map has a spatial resolution of 0.26 kpc and we find $R_{2.2} = 2.2$ kpc, $V_{2.2} = 340$ km s^{-1} and a dynamical mass of $6.0 \times 10^{10}\,\mathrm{M}_\odot$. As the Pa$\alpha$ map has a higher spatial resolution, we use this as $R_{2.2}$; this is consistent with the radius of the H I disc found by Dwarakanath et al. (1994). We thus find the dynamical mass within $R_{2.2}$ to be $M_{\mathrm{dyn},2.2} = 6.0 \times 10^{10}\,\mathrm{M}_\odot$.

3.3 Cold molecular emission

In Fig. 9, we show the CO(2–1) spectrum of Hydra-A which shows a strong and broad line present within the cluster. This detection is

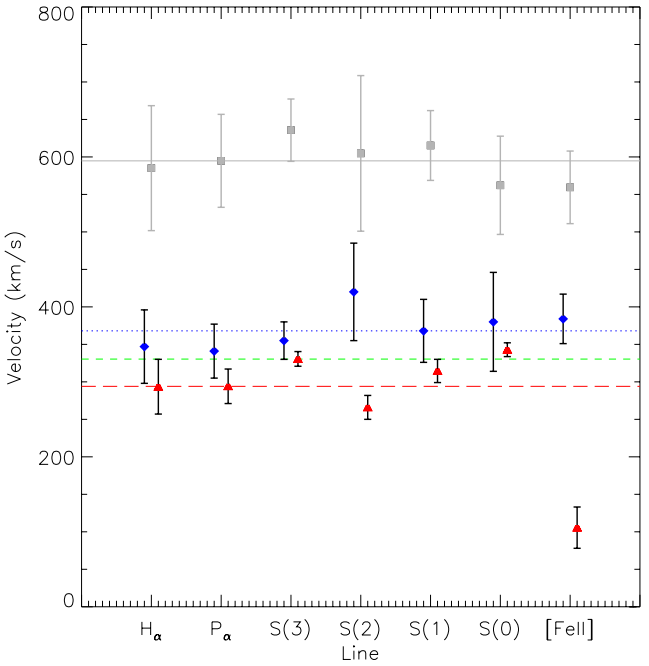

Figure 8. A comparison of the rotation velocity predicted by the disc fits for each line. The red triangles show the magnitude of the maximum velocity measured from the data, the long dashed red line shows the median of these values and the dashed green line shows the median corrected for the median inclination. The blue diamonds show the values of $V_{2.2}$ derived from the models with the dotted blue line set at the median $V_{2.2}$. The squares show the asymptotic velocity from the best-fitting model for each line with the solid line representing their median. All error bars are 1σ, and it can be seen that within errors the value of $V_{2.2}$ is consistent with the inclination-corrected maximum measured velocity.

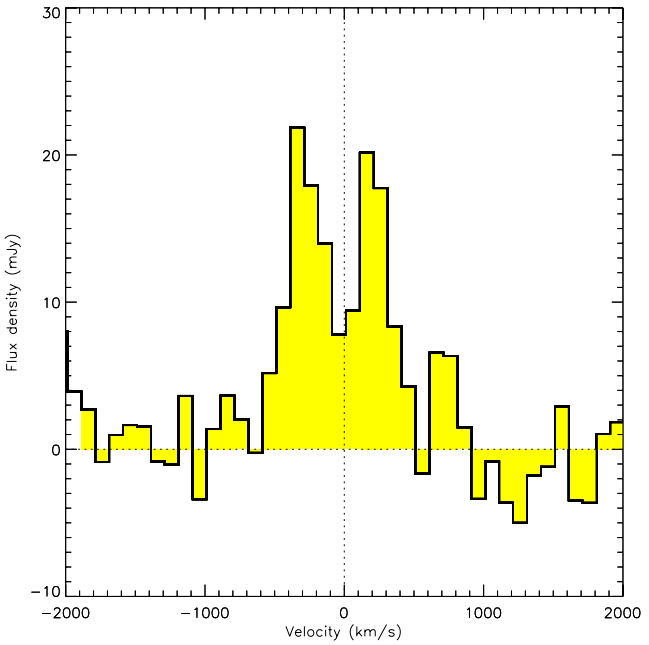

Figure 9. CO(2–1) spectrum of Hydra-A taken from the WILMA backend on IRAM 30 m. The line shows a width of 600–700 km s^{-1} consistent with the rotation velocity seen in ionized lines. A double-peaked structure is present with the trough between peaks situated at the dynamical centre of the system.

notable for several reasons, primarily the remarkable width of the line. The full width at zero intensity of 1200 km s^{-1} is comparable to the bandwidth of the past attempts to detect CO in this system (O'Dea et al. 1994; Edge 2001; Salomé & Combes 2003) so it would have been impossible to detect the full line flux before the advent of the wide-bandwidth receivers such as EMIR. The line is broader than all previous CO detections in BCGs by a factor of 30 per cent and it suggests that there may be a potentially significant number of systems that have escaped detection due to their intrinsic line width.

The spectrum also points to considerable velocity structure within the line. There are only three published double-peaked CO detections in BCGs [3C31 and 3C264 in Lim et al. (2000) and 3C84 in Salomé et al. (2011)] so the discovery of a third in a 3C radio galaxy points to a potential connection between powerful radio emission and cold gas discs. This connection extends to other radio galaxies, such as 3C236 (Labiano et al. 2013) where a molecular gas disc is found.

The total CO(2–1) line intensity is 1.87 ± 0.24 K km s^{-1} in units of measured antenna temperature ($T_{\rm A}^{*}$) or 2.79 ± 0.36 K km s^{-1} in units of main beam temperature using the conversion factor of 1.49 at the observed frequency of CO(2–1) (218.545 GHz). Following Solomon et al. (1997), the CO luminosity is given by

$$L'_{\rm CO} = 23.5 I_{\rm CO} \Omega_{\rm s} * b \frac{D_{\rm L}^2}{(1+z)^3} \quad (4)$$

with $L'_{\rm CO}$ in K km s^{-1} pc^2. Here $I_{\rm CO}$ is the main beam temperature, Ω_{s*b} is the solid angle of the source convolved with the beam and $D_{\rm L}$ is the luminosity distance of the source. Assuming that the CO emission comes from the region seen in the IFU maps shown in Section 3.1, then the source is much smaller than the beam and we can use the approximation $\Omega_{\rm s} * b \propto \Omega_{\rm b}$ which is 144 arcsec^2 for CO(2–1). The source redshift is $z = 0.054\,878$ which implies a luminosity distance of $D_{\rm L} = 242$ Mpc. This gives a CO luminosity of $L'_{\rm CO} = 4.71 \pm 0.61 \times 10^8$ K km s^{-1} pc^2, and assuming that the CO is thermally excited then $L'_{\rm CO(1-0)} = L'_{\rm CO(2-1)}$ [which is consistent with our marginal detection of CO(1–0)]. We then compute the H_2 mass using $M_{\rm H_2} = \alpha L'_{\rm CO}$ assuming a standard conversion factor of 3.0×10^{20} cm^{-2} (K km s^{-1})$^{-1}$. This corresponds to an α of 4.8 which implies a molecular gas mass of $2.26 \pm 0.29 \times 10^9$ M$_\odot$. This gas mass is comparable to the gas mass found in most other CO detected BCGs (Edge 2001; Salomé & Combes 2003), some giant ellipticals such as 3C236 (Labiano et al. 2013) and is consistent with the dynamical mass of the disc ($M_{\rm dyn,2.2} = 6.0 \times 10^{10}$ M$_\odot$).

Finally, there is significant radio continuum at both 3 and 1 mm detected as an excess baseline in the EMIR observations (285 ± 30 and 128 ± 18 mJy at 3 and 1 mm, respectively). This emission is consistent with recent high-frequency observations of the core and lobes with Multiplexed SQUID TES Array at Ninety GHz (MUSTANG) on the Green Bank Telescope (GBT; Cotton et al. 2009) and implies that the vast majority, if not all, of the detected 850 μm Submillimetre Common-User Bolometer Array (SCUBA) flux of 69.3 mJy (Zemcov et al. 2007) is from the radio continuum and not from dust emission.

3.4 Atomic gas

We show the [O I] spectrum of Hydra-A taken with *Herschel* in Fig. 10. The spectrum shows a striking similarity to the velocity structure of the CO(2–1) line implying that they trace the same cold gas clouds. This correspondence between atomic and CO velocity profiles has also been observed in other BCGs at the centre of cooling flows (for example A1068 and A2597; Edge et al.

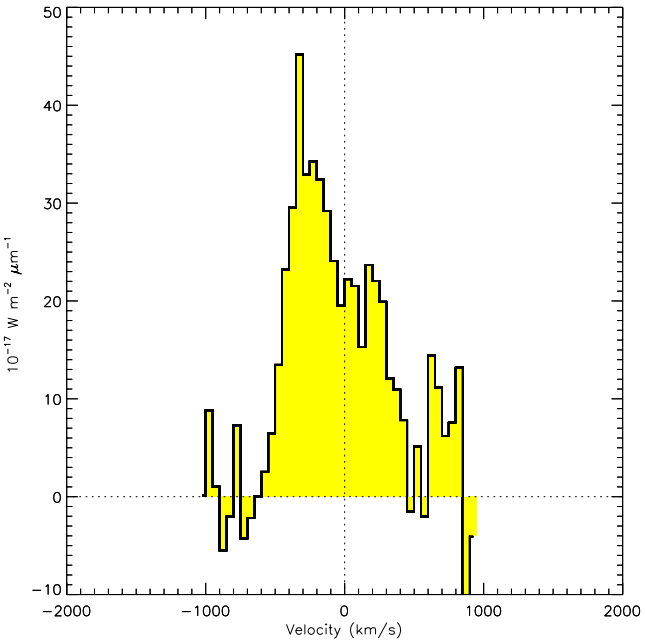

Figure 10. Far-infrared [O I] spectrum of Hydra-A taken with the PACS spectrometer on the *Herschel* space telescope. The width and structure of the line are consistent with the CO(2–1) although the ratio of the flux in the two peaks is different between the two lines.

2010; Tremblay et al. 2012). We note, however, that the [O I] line is substantially more asymmetric than the CO(2–1); we discuss this asymmetry in more detail in Section 4.3. The intrinsic velocity resolution of the PACS spectrograph at the longest wavelengths makes it harder to match the velocity structure of the [C II] line (Edge et al. 2010). However, if the CO(2–1) and [O I] lines are smoothed to the intrinsic resolution of PACS at [C II], then the three lines are consistent.

From these observations, it is possible to estimate the mass of atomic gas present in the BCG. Following Wolfire, Tielens & Hollenbach (1990), and assuming the cooling rate and C^+ abundance determined therein, one can estimate the atomic gas mass as deduced from [C II] to be

$$M_{\rm H\,I} = 2.7 \times 10^6 \left(\frac{D}{\rm Mpc}\right)^2 \left(\frac{F_{\rm [C\,II]}}{10^{-17}\,{\rm W\,cm^{-2}}}\right) {\rm M_\odot}, \quad (5)$$

where D is the distance to the cluster in Mpc and $F_{\rm [C\,II]}$ is the flux of [C II] in W cm^{-2}. We measure a [C II] flux of 5.3×10^{-21} W cm^{-2} and use a distance of 242 Mpc, which gives an atomic gas mass of 8.4×10^7 M$_\odot$. The assumptions going into this estimate make it rather uncertain (perhaps by as much as an order of magnitude) but this mass is just below the upper limit of 4×10^8 M$_\odot$ derived from H I absorption by Dwarakanath et al. (1994).

3.5 Star formation and dust

The dust lane visible in the *HST* imaging suggests that a substantial mass of dust must be present within the disc. Oonk et al. (in preparation) calculate the dust mass within the BCG to be 5.5×10^6 M$_\odot$, at a temperature of 26 K, which corresponds to a gas-to-dust ratio of ∼400. However, the dust emission is unresolved with PACS at the shortest wavelength so the dust is not extended on scales of >5 arcsec. This gas-to-dust ratio is higher than in spiral galaxies with gas discs such as the Milky Way or those in the Spitzer Infrared Nearby Galaxies Survey (SINGS; gas-to-dust ratios of ∼150 and ∼200, respectively; Draine et al. 2007), suggesting that the dust is more diluted in Hydra-A. However, it is important to note the uncertainties on both the gas and dust mass when making this comparison. The standard conversion factor from the CO line intensity to molecular gas mass assumes that the gas has conditions (excitation, density, temperature and metallicity) similar to molecular clouds in the Milky Way. There is also some uncertainty in the dust mass given that its estimation is very model dependent, and either of which could account for this difference. Therefore, a factor of 2 in the gas-to-dust ratio is not sufficient to draw any general conclusions about the nature of the dust in Hydra-A.

The origin of the large mass of molecular gas within the system is best explained through the direct cooling of hot gas from the ICM as gas-rich mergers are rare (Kirkpatrick et al. 2009) and gas from stellar mass-loss is most likely to be assimilated into the ICM (Mathews 1990), see Section 4.1. However, in this scenario the origin of the dust is not clear. It is possible that the dust forms directly in the cold clouds deposited by the cooling flow (Fabian, Johnstone & Daines 1994) or from stellar mass-loss (Voit & Donahue 2011). While both would produce less dust and therefore a higher gas-to-dust ratio, the direct evidence for either is marginal (Rawle et al. 2012). Another possibility is that the dust is produced by the star formation within the disc but it requires a relatively fast pollution of the gas with dust to explain the observed gas-to-dust ratio.

The Hydra-A BCG has a published star formation rate of ∼2–3 M$_\odot$yr^{-1} from both UV and MIR observations (Donahue et al. 2011; Hoffer et al. 2012). The UV image presented in Fig. 1 shows clear clumps of UV emission with a lack of UV from the region of the disc. The concentration of dust in the gas disc could easily obscure the UV emission from that region so it is likely that star formation is occurring in, and close to, the disc.

4 DISCUSSION

The results presented above build directly on the previous studies of Hydra-A and confirm unambiguously that there is a coherent and large-amplitude velocity gradient (∼700 km s^{-1}) in the gaseous disc across the galaxy. Importantly, the major axis of this velocity gradient is aligned perpendicular to the axis of the cavities formed by the radio jets (Figs 1 and 11), similar to the alignment seen in other BCGs (Wilman, Edge & Swinbank 2009; Oonk et al. 2010). This strongly suggests that the angular momentum of the gas on large scales influences the flow of gas close to the black hole and the generation of jets (Baum, Heckman & van Breugel 1992; Prandoni et al. 2010). The addition of the multiple molecular and atomic line detections allows us to connect the cold gas to the observed emission line dynamics from IFU observations. The double-peaked velocity profile seen in both the CO and [O I] lines is consistent with the cold gas being distributed throughout the disc. This match extends to both the ionized hydrogen (traced by Paα) and [O I] gas sharing a significant asymmetry to the blue that appears to be localized to the western edge of the gas disc.

The prominence of the gas disc in Hydra-A is accentuated by the fact that it is being viewed close to edge-on and exhibits a striking dust lane in *HST*- (fig. 1, Mittal et al., in preparation) and ground-based imaging (Ramos Almeida et al. 2011). Similar gas discs are known in other BCGs at the centre of cooling flows, e.g. NGC 1275/3C84 in the Perseus cluster (Wilman, Edge & Johnstone 2005; Lim, Ao & Dinh-V-Trung 2008) and NGC 383/3C31 (Lim et al. 2000; Okuda et al. 2005; Ocaña Flaquer et al. 2010). The prevalence of these discs in radio luminous systems is suggestive of a link between large-scale gas discs and AGN activity but may

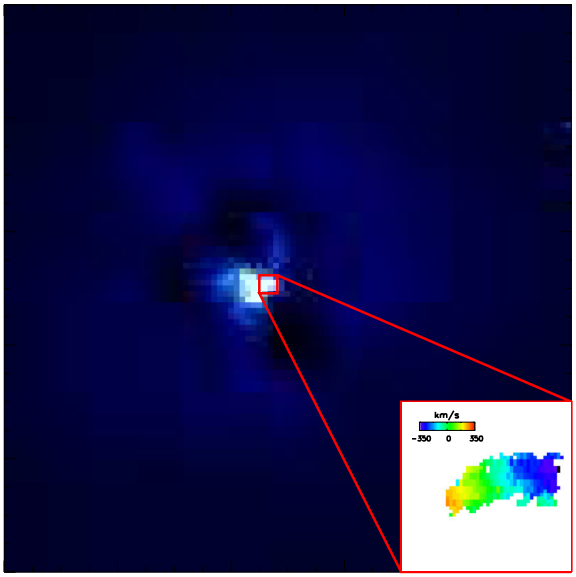

Figure 11. The central $\sim 3 \times 3$ arcmin^2 region of the Hydra-A cluster shown in an unsharp masked 221 ks integration X-ray image. Two depressions in the X-ray emission show the location of cavities $\sim$20 arcsec to the north and south of the cluster centre. The inset shows the Paα velocity field in an $\sim 6 \times 6$ arcsec^2 region centred on the BCG as derived from single-component fits to the Paα line in Hydra-A. The velocity field is with respect to the zero-point of the nominal cluster redshift of $z = 0.0549$. The velocity field shows an east–west alignment almost perpendicular to the alignment of the X-ray cavities.

be an observational selection effect as many of the galaxies with known discs were selected for *HST* imaging on the basis of their radio power (de Koff et al. 2000; Verdoes Kleijn & de Zeeuw 2005; Tremblay et al. 2007).

The gas distribution within the disc as a function of radius cannot be unambiguously determined from our current data so the innermost extent of the gas and whether it is continuous with radius are open issues. Only high spatial resolution imaging of optically thin lines that are unaffected by obscuration will be able to address the nature of the gas close to the Bondi radius and the inner stable orbit of the gas (Prandoni et al. 2010).

4.1 Fuelling the feedback?

Hydra-A offers several significant insights into the nature of cooling flows and AGN feedback. The discovery of a distinct disc of cold gas in such a powerful radio galaxy can be used to assess the energetics and fuelling of AGN activity.

Studies of the cavities in the ICM in several cluster cores indicate that a substantial amount of energy is being transferred from the AGN into the surrounding gas through the mechanical work done by the radio lobes (McNamara et al. 2001; McNamara & Nulsen 2007). The total energy of the outbursts is of the order of 10^{61} erg which corresponds to the accretion of 10^7 M$_\odot$ of gas (at a rate of 0.1–0.25 M$_\odot$ yr^{-1}) on to the central super massive black hole assuming an efficiency of 0.1 (Wise et al. 2007). Combining our estimates of the gas masses in the various phases, we calculate the total mass of cold gas in the disc to be $2.3 \pm 0.3 \times 10^9$ M$_\odot$. Oonk et al. (in preparation) calculate that the dust mass is 5.5×10^6 M$_\odot$ at a temperature 26 K, though it is important to note that dust mass estimates are highly model dependent. Assuming that the dust lane in the disc contains the majority of this cold material, then it has a total mass of $2.3 \pm 0.3 \times 10^9$ M$_\odot$, which is sufficient to fuel a future outburst of comparable magnitude. We note, however, that the infall time for gas in the disc will be large and that any gap within the inner disc could inhibit gas accretion.

While this comparison is by no means proof that the cold gas was solely responsible for the fuelling of any outburst in Hydra-A, other systems may provide clues. Edge (2001) notes that the BCGs with the most powerful extended radio emission (Cygnus-A, Perseus-A, M87 and Hercules-A) are less luminous in CO for their given optical line luminosity. If the radio emission is generated by the rapid depletion of the gas in the core of the galaxy, then this could explain the weaker molecular gas emission.

The origin of the cold gas is another open question. While the accretion of cold gas from infalling cluster members and through stellar winds can be invoked for lower luminosity systems like M87 and NGC 4696 (Sparks, Macchetto & Golombek 1989; Sparks et al. 2004), these stochastic and ad hoc processes struggle to explain the observation that the vast majority of BCGs in cooling flows exhibit optical line emission (Crawford et al. 1999; Cavagnolo et al. 2008) and CO lines (Edge 2001; Salomé & Combes 2003) when the central cooling time or entropy is low, particularly given the large gas masses ($>10^{10.5}$ M$_\odot$) found in many systems. Instead, X-ray observations allow for residual gas cooling that is not truncated by the AGN feedback which can still be significant (Wise et al. 2007; Sanders & Fabian 2011), and the 10–100 M$_\odot$ yr^{-1} observed in the strongest cooling flows can result in the accumulation of sufficient cold gas in $\sim 10^9$ yr. This reasonably constant supply of cold gas could in principle power the cores of all BCGs in the strongest cooling flows all the time. The observation that all strong cooling flows have a radio source (Mittal et al. 2009) may be an indication that this consistent accumulation of fuel for powering the black hole and star formation is indeed the case.

If the accretion of cold gas deposited from the cooling of intracluster gas is the dominant accretion mode in cluster cores, then what properties do we expect other systems to share with Hydra-A? The very large dust disc and the extremely broad line width in Hydra-A may be the product of a preferential viewing angle where the cold disc of gas and dust is being observed almost edge-on (Fig. 1). This fortuitous viewing angle also maximizes the visibility of the X-ray cavities if they are created perpendicular to the disc. NGC 1275 does not show a similar dust lane but the presence of an inner spiral structure and a direct line of sight to the nuclear emission implies that we are viewing any disc at close to face-on ($<30^\circ$).

Finally, the observation of a disc implies that the cold gas has significant angular momentum with respect to the central galaxy. If the central galaxy is at rest in the cluster and any gas cooling is symmetric, then the angular momentum of the cold gas should be small. However, optical observations of clusters show that the central galaxy is frequently offset from the cluster mean (Zabludoff et al. 1993; Bird 1994), and X-ray observations imply that large-scale bulk motion, or 'sloshing', is common in the ICM (Markevitch & Vikhlinin 2007; ZuHone, Markevitch & Johnson 2010). Therefore, the presence of angular momentum in the cold gas phase is not a surprise on scales beyond the Bondi radius. However, this angular momentum poses a 'centrifugal barrier' to gas accretion within it (Narayan & Fabian 2011; McNamara & Nulsen 2012) so constraining how the gas moves within the disc is an important observational challenge.

4.2 The blueshifted line emission

The extended, one-sided nature of the blueshifted Paα line component (see region 2 in Fig. 3) implies that this emission is from gas that is not directly related to the gas disc or the disc is asymmetric. In NGC 1275 gas on 5–20 kpc scales is observed which does not follow the rotation observed on smaller scales (Lim et al. 2008; Salomé et al. 2008; Mittal et al. 2012) so the presence of gas that has a substantial offset from the systemic velocity of the BCG is not unprecedented. Indeed, there are systems where the majority of the optical line emission lies off the BCG spatially and in velocity, such as A1991 and Ophiuchus (Hamer et al. 2012). In these cases, the peak of the X-ray emission is coincident with the line emission and not on the BCG. In the case of Hydra-A, the X-ray emission close to the BCG is strongly affected by the radio cavities but there is a relatively weak excess to the west of the BCG (Sambruna et al. 2000; Wise et al. 2007).

What are the possible origins of this additional gas component? One possibility is that it is related to the merger of another gas-rich galaxy with the BCG. However, we view this scenario as unlikely given the relatively large gas mass involved and the lack of any donor galaxy in the cluster core. The inference that the cold gas found in the cores of most clusters is related to gas cooling rather than a merger with a gas-rich galaxy has been the subject of extensive debate over the past three decades (Sparks 1992; Edge 2001) but the close connection between the X-ray properties of the cluster core and the optical, infrared and radio properties of the BCG which is seen in the vast majority of systems clearly favours a sustained and non-stochastic explanation (Cavagnolo et al. 2008; O'Dea et al. 2008; Voit et al. 2008; Sanderson et al. 2009). Therefore, the origin of the cold gas from the direct cooling of the ICM best matches the observations.

One implication of the gas cooling from the ICM is that it will retain the velocity of the cluster and not necessarily that of the BCG. So, if the BCG is not at rest with respect to the cluster, then in principle it is possible that two velocity components could be observed, one associated with the cluster and one with the BCG. This could potentially explain the second component seen in the Paα. To test whether this is the case in Hydra-A, we extract the galaxies known within 15 arcmin (940 kpc) from the NASA/IPAC Extragalactic Database and find 20 potential cluster members (other than Hydra-A itself) and the mean redshift for these is 0.0529 or 450 km s^{-1} lower than Hydra-A and comparable to the blueshifted line component. Some caution is required in interpreting this result given that the number of galaxies is relatively small and that there is a second cluster of galaxies present (probably associated with Abell 780 that lies 11 arcmin from Hydra-A and is frequently, and completely erroneously, equated to Hydra-A in the literature). However, there is some evidence that the second gas component could be related to the cluster velocity giving a natural explanation as to why two velocity components are present.

This conclusion requires the BCG to have a significant velocity with respect to the cluster. There is a considerable amount of literature on 'speeding cDs' (Beers & Geller 1983; Zabludoff et al. 1993; Pimbblet, Roseboom & Doyle 2006) and there is a significant fraction of clusters with a velocity offset between the cluster mean and the BCG velocities of more than 300 km s^{-1}. The origin of this velocity offset is poorly understood but probably relates to a recent merger of a substantial subcluster that affects the cluster mean velocity with respect to the BCG (Fujita, Sarazin & Sivakoff 2006). The presence of cold fronts and merger shocks could be used to support this interpretation (Markevitch & Vikhlinin 2007; ZuHone, Markevitch & Johnson 2010; ZuHone, Markevitch & Lee 2011). However, these are most prominent for mergers in the plane of the sky, whereas the observed velocity difference will be largest for mergers along the line of sight so the lack of these features does not exclude the presence of a significant merger.

The implications for the interpretation of other clusters are significant. For instance, A1795 has a broad CO velocity width (Salomé & Combes 2003) and a prominent tail of Hα line emission (O'Dea et al. 2004; Crawford, Sanders & Fabian 2005; McDonald & Veilleux 2009). The BCG in A1795 is known to be offset from the cluster mean (Oegerle & Hill 1994) and there is evidence for a merger from the X-ray imaging (Ettori et al. 2002). Also the velocity offsets between the stellar component of the BCG, the cold gas retained by the BCG, the mean of the cluster members and the cold gas outside the influence of the BCG all need to be considered separately. The gaseous nature of the ICM and cold molecular gas mean that they can experience shocks and decouple from the dark matter and stellar components which are relatively collisionless and respond only to gravity. Therefore, it is possible that all four components could differ in velocity, with the BCG and cluster mean having the widest separation and the gas components sitting between them. Accurate measurements of the stellar and ionized gas components of BCGs are relatively straightforward to obtain (e.g. Crawford et al. 1999) as are similar measures of the molecular and cool atomic gas. However, determining the mean velocity of cluster members requires at least 50 cluster members to ensure a statistically robust value so dedicated multi-object spectroscopy is required which has more demanding observing time requirements.

One concern with this interpretation is that gas kinematics in this region remain consistent with the rotating disc rather than appearing as a separate kinematic component. The other possible explanation of the second peak in the Paα flux map is that there is some asymmetry in the disc. We note that the H_2 (1–0) S series lines do not detect this second component at greater than 5σ significance (see Fig. 4), suggesting that the gas may be more ionized at the western edge of the disc. The presence of a bright region of UV emission near this second peak (see region 2 in the left-hand panel of Fig. 1) could potentially account for a higher fraction of ionized gas in this region (see Section 4.3 for discussion on the balance of gas phases). Another possible explanation for an asymmetry in the disc is that it is the result of gas which has been lifted out of the central regions. The excavation of material from BCGs by radio jets has been seen in several systems (e.g. Perseus, Fabian et al. 2003b; Abell 2052, Blanton et al. 2001) and if occurring on small scales here could produce an asymmetry in the disc on the scales seen. While the radio map shown in Fig. 1 (Taylor et al. 1990; Sambruna et al. 2000) does show an extent to the north-west which matches the position and direction of blueshifted emission, Taylor et al. (1990) identify this as an artificial feature produced by phase errors.

4.3 The balance of molecular, atomic and ionized gas

The SINFONI data provide a direct comparison of the molecular and ionized gas in Hydra-A from the Paα and (1–0) S series H_2 molecular lines. The presence of a secondary peak in the Paα which is not present in the warm molecular gas at above 5σ suggests that the western edge of the disc is either less molecular or cooler than the rest of the disc.

In order to compare the cold molecular, atomic and ionized gas directly, we produced a reconstructed spectrum of the Paα by taking the measured velocity, line width and flux of the emission at each

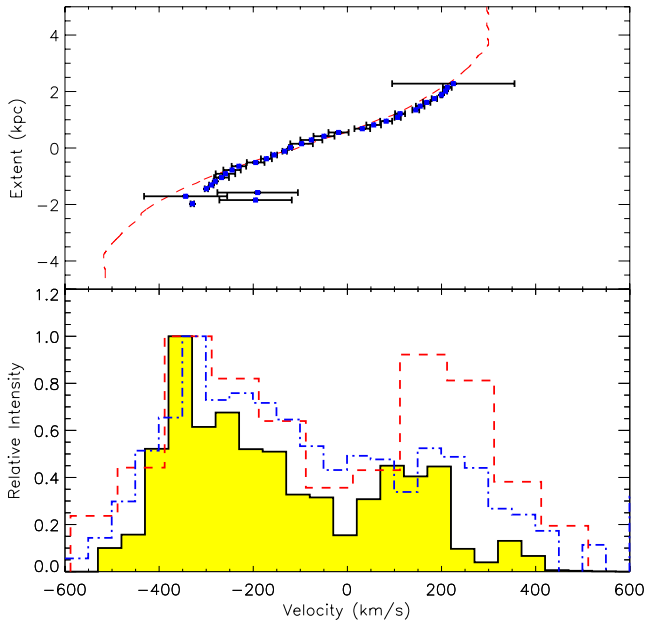

Figure 12. The Paα velocity profile along with a reconstructed spectrum. The reconstructed spectrum of the Paα bears a remarkable resemblance to those of the atomic (blue dot–dashed line) and molecular (red dashed line) line profiles. The Paα profile shows an asymmetry with more pronounced blue peak similar to that of the [O I] suggesting that they trace similar gas distributions. Note that all three show a double-peaked structure with a similar separation indicating that the CO and [O I] share the same velocity structure as the Paα.

point used to produce the velocity profile and created a Gaussian with these parameters. The spectra of these individual points were then summed to give the final spectrum of the Paα emission before being binned to a level comparable to the CO and [O I] spectra (50 km s^{-1}). As this reconstructed spectrum is produced from the emission detected by the fitting routine, it only includes the high surface brightness ($\geq 7\sigma$ significance) Paα emission. A comparison of the CO, [O I] and reconstructed Paα integrated line velocity profiles is shown in Fig. 12. We note that the Paα and [O I] line profiles are substantially more asymmetric than the line profile of the CO. For the Paα, we attribute this to the secondary flux peak towards the western (blueshifted) edge of the disc, possibly related to the cooling flow (see Section 4.2). The [O I] profile shares a similar asymmetry to the Paα suggesting that they are emitted by gas clouds sharing the same spatial distribution. The more symmetric appearance of the CO profile suggests that it lacks a significant extra component, much as the (1–0) S series H_2 molecular lines do.

However, despite this it can be seen that the three profiles are remarkably consistent with each other. All three profiles show a double-peaked profile with a consistent separation between the peaks. We note that the Paα line appears narrower than the CO and [O I]. While this difference may be real, it may also be an effect of the different spatial scales from which these spectra were extracted. Both the CO and [O I] profiles are extracted from regions of the order of 10×10 arcsec^2 ($\sim$10 arcsec beam for the CO and the [O I] pixels; scale is $\sim$10 arcsec). By contrast, the Paα profile is reconstructed from the 7σ fits (a region of $\sim 5 \times 2$ arcsec^2) and thus has a sharp cut-off at low surface brightness.

Therefore, we infer that the gas on the western edge of the disc does contain cold molecular gas implying that the non-detection of the warm, vibrationally excited molecular line emission is related to the excitation of the gas not the absence of molecular gas. This difference in excitation could be due to lower shock heating (Jaffe, Bremer & van der Werf 2001; Wilman et al. 2002), less direct, radiative AGN heating away from the centre of the galaxy or the gas is more directly related to the star formation in the nearby UV bright region (see Fig. 1). However, equally large differences are seen in the ratio of Paα and the molecular lines in IFU observations of other systems with stronger cold molecular emission away from the central galaxy (Wilman et al. 2009; Oonk et al. 2010) and the ratio varies significantly between sources (Edge et al. 2002) so one cannot draw universal conclusions from the line ratios in Hydra-A alone.

5 SUMMARY

Mechanical feedback provided by AGN outbursts from BCGs is commonly believed to be the main contributing factor which prevents the catastrophic cooling of gas within cluster cores. For this process to work effectively, a mechanism of self-regulation is required to maintain the balance between the cooling gas and the feedback. This requires a direct link between the cooling gas (on kpc scales) and its supply to the super massive black hole be established which results in the activation of the AGN once cooling reaches a critical threshold. Here we study Hydra-A, a well-known BCG in which AGN feedback appears to be currently active. We present clear evidence for a kpc-scale rotating disc of ionized and warm molecular gas. In addition, the agreement between the integrated line profile of the cold molecular and atomic lines and the ionized and warm molecular gas traced in the optical and NIR IFU observations (Fig. 12) implies that the cold gas follows a similar ordered rotation. The axis of this rotation appears parallel to the axis along which the AGN is inflating cavities within the cluster core.

It is important to remember that for a single object this alignment could simply be coincidental so a larger more statistically representative sample is needed. However, it is suggestive given the presence of similar CO profiles and known molecular discs in other powerful radio galaxies (see Section 3.3). It hints at a possible connection between the angular momentum of gas cooling on kpc scales and the formation of the radio jets in the AGN. The existence of a relatively thin ($<$1 kpc) disc that has a velocity range of $>$700 km s^{-1} has profound implications for our understanding of Hydra-A in particular and radio galaxies in general.

ACKNOWLEDGEMENTS

SLH acknowledges the support received from an STFC studentship and the European Research Council for Advanced Grant Program num 267399-Momentum. AMS gratefully acknowledges an STFC Advanced Fellowship through grant ST/H005234/1. ACE acknowledges support from STFC grant ST/I001573/1.

This work is based on observations made with ESO Telescopes at the La Silla or Paranal Observatories under programme IDs 080.A-0224 and 082.B-0671

Herschel is an ESA space observatory with science instruments provided by European-led Principal Investigator consortia and with important participation from NASA.

This work is also based on observations made with the NASA/ESA *Hubble Space Telescope*, obtained from the data archive at the Space Telescope Institute. STScI is operated by the

association of Universities for Research in Astronomy, Inc., under the NASA contract NAS 5-26555.

Also, observations were carried out with the IRAM 30 m Telescope. IRAM is supported by INSU/CNRS (France), MPG (Germany) and IGN (Spain)

The National Radio Astronomy Observatory is a facility of the National Science Foundation operated under cooperative agreement with Associated Universities, Inc.

REFERENCES

Baum S. A., Heckman T. M., van Breugel W., 1992, ApJ, 389, 208
Bautista M. A., Pradhan A. K., Osterbrock D. E., 1994, ApJ, 432, L135
Beers T. C., Geller M. J., 1983, ApJ, 274, 491
Binney J., Tremaine S., 1987, Galactic Dynamics. Princeton Univ. Press, Princeton, NJ
Bird C. M., 1994, AJ, 107, 1637
Blanton E. L., Sarazin C. L., McNamara B. R., Wise M. W., 2001, ApJ, 558, L15
Böhringer H., Voges W., Fabian A. C., Edge A. C., Neumann D. M., 1993, MNRAS, 264, L25
Bower R. G., Benson A. J., Malbon R., Helly J. C., Frenk C. S., Baugh C. M., Cole S., Lacey C. G., 2006, MNRAS, 370, 645
Carter M. et al., 2012, A&A, 538, A89
Cavagnolo K. W., Donahue M., Voit G. M., Sun M., 2008, ApJ, 683, L107
Cotton W. D. et al., 2009, ApJ, 701, 1872
Courteau S., 1997, AJ, 114, 2402
Crawford C. S., Allen S. W., Ebeling H., Edge A. C., Fabian A. C., 1999, MNRAS, 306, 857
Crawford C. S., Sanders J. S., Fabian A. C., 2005, MNRAS, 361, 17
Croton D. J. et al., 2006, MNRAS, 365, 11
de Koff S. et al., 2000, ApJS, 129, 33
Donahue M., de Messières G. E., O'Connell R. W., Voit G. M., Hoffer A., McNamara B. R., Nulsen P. E. J., 2011, ApJ, 732, 40
Draine B. T. et al., 2007, ApJ, 663, 866
Dwarakanath K. S., van Gorkom J. H., Owen F. N., 1994, ApJ, 432, 469
Dwarakanath K. S., Owen F. N., van Gorkom J. H., 1995, ApJ, 442, L1
Edge A. C., 2001, MNRAS, 328, 762
Edge A. C., Wilman R. J., Johnstone R. M., Crawford C. S., Fabian A. C., Allen S. W., 2002, MNRAS, 337, 49
Edge A. C. et al., 2010, A&A, 518, L46
Egami E., Rieke G. H., Fadda D., Hines D. C., 2006, ApJ, 652, L21
Ekers R. D., Simkin S. M., 1983, ApJ, 265, 85
Ettori S., Fabian A. C., Allen S. W., Johnstone R. M., 2002, MNRAS, 331, 635
Fabian A. C., 2012, ARA&A, 50, 455
Fabian A. C., Hu E. M., Cowie L. L., Grindlay J., 1981, ApJ, 248, 47
Fabian A. C., Johnstone R. M., Daines S. J., 1994, MNRAS, 271, 737
Fabian A. C., Sanders J. S., Allen S. W., Crawford C. S., Iwasawa K., Johnstone R. M., Schmidt R. W., Taylor G. B., 2003a, MNRAS, 344, L43
Fabian A. C., Sanders J. S., Crawford C. S., Conselice C. J., Gallagher J. S., Wyse R. F. G., 2003b, MNRAS, 344, L48
Freeman K. C., 1970, ApJ, 160, 811
Fujita Y., Sarazin C. L., Sivakoff G. R., 2006, PASJ, 58, 131
Hamer S. L., Edge A. C., Swinbank A. M., Wilman R. J., Russell H. R., Fabian A. C., Sanders J. S., Salomé P., 2012, MNRAS, 421, 3409
Hansen L., Jorgensen H. E., Norgaard-Nielsen H. U., 1995, A&A, 297, 13
Hoffer A. S., Donahue M., Hicks A., Barthelemy R. S., 2012, ApJS, 199, 23
Jaffe W., Bremer M. N., 1997, MNRAS, 284, L1
Jaffe W., Bremer M. N., van der Werf P. P., 2001, MNRAS, 324, 443
Kirkpatrick C. C. et al., 2009, ApJ, 697, 867
Labiano A. et al., 2013, A&A, 549, A58
Lim J., Leon S., Combes F., Dinh-V-Trung, 2000, ApJ, 545, L93
Lim J., Ao Y., Dinh-V-Trung, 2008, ApJ, 672, 252
Markevitch M., Vikhlinin A., 2007, Phys. Rep., 443, 1
Mathews W. G., 1990, ApJ, 354, 468
McDonald M., Veilleux S., 2009, ApJ, 703, L172
McDonald M., Veilleux S., Rupke D. S. N., Mushotzky R., 2010, ApJ, 721, 1262
McNamara B. R., 1995, ApJ, 443, 77
McNamara B. R., Nulsen P. E. J., 2007, ARA&A, 45, 117
McNamara B. R., Nulsen P. E. J., 2012, New J. Phys., 14, 055023
McNamara B. R. et al., 2000, ApJ, 534, L135
McNamara B. R. et al., 2001, ApJ, 562, L149
Melnick J., Gopal-Krishna, Terlevich R., 1997, A&A, 318, 337
Miller S. H., Bundy K., Sullivan M., Ellis R. S., Treu T., 2011, ApJ, 741, 115
Mittal R., Hudson D. S., Reiprich T. H., Clarke T., 2009, A&A, 501, 835
Mittal R. et al., 2011, MNRAS, 418, 2386
Mittal R. et al., 2012, MNRAS, 426, 2957
Narayan R., Fabian A. C., 2011, MNRAS, 415, 3721
O'Dea C. P., Baum S. A., Maloney P. R., Tacconi L. J., Sparks W. B., 1994, ApJ, 422, 467
O'Dea C. P., Baum S. A., Mack J., Koekemoer A. M., Laor A., 2004, ApJ, 612, 131
O'Dea C. P. et al., 2008, ApJ, 681, 1035
Ocaña Flaquer B., Leon S., Combes F., Lim J., 2010, A&A, 518, A9
Oegerle W. R., Hill J. M., 1994, AJ, 107, 857
Okuda T., Kohno K., Iguchi S., Nakanishi K., 2005, ApJ, 620, 673
Oonk J. B. R., Jaffe W., Bremer M. N., van Weeren R. J., 2010, MNRAS, 405, 898
Peterson J. R. et al., 2001, A&A, 365, L104
Pilbratt G. L. et al., 2010, A&A, 518, L1
Pimbblet K. A., Roseboom I. G., Doyle M. T., 2006, MNRAS, 368, 651
Prandoni I., Laing R. A., de Ruiter H. R., Parma P., 2010, A&A, 523, A38
Ramos Almeida C., Tadhunter C. N., Inskip K. J., Morganti R., Holt J., Dicken D., 2011, MNRAS, 410, 1550
Rawle T. D. et al., 2012, ApJ, 747, 29
Salomé P., Combes F., 2003, A&A, 412, 657
Salomé P., Combes F., Revaz Y., Edge A. C., Hatch N. A., Fabian A. C., Johnstone R. M., 2008, A&A, 484, 317
Salomé P., Combes F., Revaz Y., Downes D., Edge A. C., Fabian A. C., 2011, A&A, 531, A85
Sambruna R. M., Chartas G., Eracleous M., Mushotzky R. F., Nousek J. A., 2000, ApJ, 532, L91
Sanders J. S., Fabian A. C., 2011, MNRAS, 412, L35
Sanders J. S., Fabian A. C., Frank K. A., Peterson J. R., Russell H. R., 2010, MNRAS, 402, 127
Sanderson A. J. R., Edge A. C., Smith G. P., 2009, MNRAS, 398, 1698
Simkin S. M., 1979, ApJ, 234, 56
Smith R. J. et al., 2004, AJ, 128, 1558
Solomon P. M., Downes D., Radford S. J. E., Barrett J. W., 1997, ApJ, 478, 144
Sparks W. B., 1992, ApJ, 399, 66
Sparks W. B., Macchetto F., Golombek D., 1989, ApJ, 345, 153
Sparks W. B., Donahue M., Jordán A., Ferrarese L., Côté P., 2004, ApJ, 607, 294
Taylor G. B., 1996, ApJ, 470, 394
Taylor G. B., Perley R. A., Inoue M., Kato T., Tabara H., Aizu K., 1990, ApJ, 360, 41
Tremblay G. R., Chiaberge M., Donzelli C. J., Quillen A. C., Capetti A., Sparks W. B., Macchetto F. D., 2007, ApJ, 666, 109
Tremblay G. R. et al., 2012, MNRAS, 424, 1042
Verdoes Kleijn G. A., de Zeeuw P. T., 2005, A&A, 435, 43
Voit G. M., Donahue M., 2011, ApJ, 738, L24
Voit G. M., Cavagnolo K. W., Donahue M., Rafferty D. A., McNamara B. R., Nulsen P. E. J., 2008, ApJ, 681, L5
Wilman R. J., Edge A. C., Johnstone R. M., Fabian A. C., Allen S. W., Crawford C. S., 2002, MNRAS, 337, 63
Wilman R. J., Edge A. C., Johnstone R. M., 2005, MNRAS, 359, 755

Wilman R. J., Edge A. C., Swinbank A. M., 2009, MNRAS, 395, 1355
Wise M. W., McNamara B. R., Nulsen P. E. J., Houck J. C., David L. P., 2007, ApJ, 659, 1153
Wolfire M. G., Tielens A. G. G. M., Hollenbach D., 1990, ApJ, 358, 116
Zabludoff A. I., Geller M. J., Huchra J. P., Vogeley M. S., 1993, AJ, 106, 1273
Zemcov M., Borys C., Halpern M., Mauskopf P., Scott D., 2007, MNRAS, 376, 1073
ZuHone J. A., Markevitch M., Johnson R. E., 2010, ApJ, 717, 908
ZuHone J. A., Markevitch M., Lee D., 2011, ApJ, 743, 16

This paper has been typeset from a TEX/LATEX file prepared by the author.